Performance study of Level2 Muon Trigger System in the ATLAS experiment

Takeshi Dohmae

Department of Physics, The University of Tokyo

8 January 2009

Abstruct

Muons are very important probe to the search of new physics at the LHC. The ATLAS experiment has developed as elaborated muon trigger system. In this thesis, a muon trigger in the Level2 trigger system (muFast) is evaluated. New algorithms are also developed and compared with the standard algorithm.

Contents

Chapter 1

Introduction

The LHC is an accelerator colliding two proton beams with the energy of 7 TeV and the total center mass energy is 14 TeV. It has just begun operation in 2008. The main aim of the LHC is the discovery of Higgs and to explore physics beyond the Standard Model such as Super Symmetry.

Many new particles have decay mode with muons in the final state. This is why the muon is one of the potential signature of new physics. On the other hand, from the proton collision, huge amount of particles are generated. Since high energy muon can penetrate thick materials and it comes out, it is easy to identify. For these reasons, measurement of muon is important in the experiment. The ATLAS detector is constructed at collision point of LHC. ATLAS detector has enormous muon spectrometer with large toroid magnets.

To reduce the trigger rate in keeping interesting physics events, ATLAS has employed a three level trigger system; Level1, Level2 and Event Filter. Muon rate at Level1 trigger is expected to be more than 10 kHz. It is required to Level 2 trigger to reduce this rate to 1kHz using precision detector information. The decision is to be issued quick. The processing time in Level 2 trigger is to be less than 10 msec on average.

The first step of the Level2 muon trigger is a standalone trigger which uses data only from the muon spectrometer. The performance of the algorithm is investigated in this thesis.

In the experiment, there are huge amount of back ground and fake from both charged and neutral particles. Fake muons might be reconstructed from hits. To reduce these fake muons, tighter coincidence between the muon detectors might help. The main purpose

of this study is to understand algorithm of current muon standalone trigger and to investigate its performance. Then new algorithms are considered and each performances are compared.

The chapter are organized as follow. A brief description of LHC and ATLAS experiment are described in Chapter 2. Chapter 3 gives details of muon trigger system. Properties of muon standalone trigger is described in Chapter4. Explanation of new algorithms, calibration and comparing are investigated in Chapter 5. Chapter 6 gives Summary.

Chapter 2

The ATLAS experiment at LHC

2.1 LHC

The Large Hadron Collider (LHC) is the proton-proton collider being constructed at CERN. The beam energy achieves to 7 TeV and the total center mass energy is 14 TeV. Its circumference is about 27 km. The ring is built in the old LEP tunnel crossing the border between Switzerland and France. The machine enables the human beings to access to the physics at TeV scale. It is also expected that the Higgs Boson which will be discovered by the experiment at LHC. In September 2007, the first beam with 450 GeV are circulated and collisions will start in summer 2009. Some typical LHC design parameters are shown in table 2.1.

Circumference of the ring	26.7 km
Proton beam energy	7 TeV
Number of particles per bunch	1.15×10^{11}
Luminosity	$10^{34}cm^{-2}s^{-1}$
Number of bunches	2808
Time between bunch crossings	25 ns
bunch crossing frequency	45 MHz

Table 2.1: Details of LHC [1]

The proton beam of 7 TeV is produced in the following way. The proton beam from linac is injected into CERN proton synchrotron reaching 25 GeV proton energy. Then the

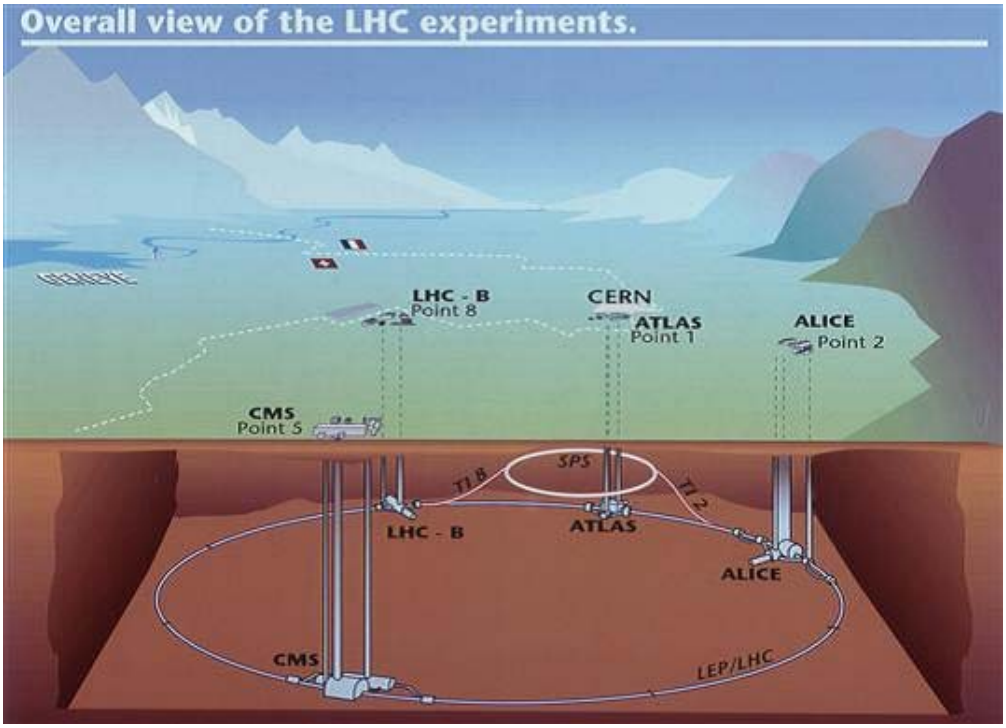

Figure 2.1: LHC and Detectors

beam is accelerated in super proton synchrotron up to 450 GeV. After that, the proton beam is injected to the LHC ring and accelerated up to 7 TeV. The overall of LHC is shown in Figure 2.1.

To confine the 7 TeV proton beam in the ring, it is necessary to produce a strong magnetic field. It is achieved by the 1,232 of superconducting dipole magnets. The conductor of the magnet is made of Niobium-titanium. The magnets are cooled down to 1.9 K by super fluid helium. And they enables to provide 8.33 Tesla of magnetic field.

There are four main experiments at the LHC; ATLAS, CMS, ALICE, and LHCb. ATLAS and CMS use general purposed detectors for vast physics to pico including Higgs search, physics at TeV scale and so on. ALICE detector is specialized for high energy heavy ion collisions to study,for example, quark gluon plasma. LHCb studies of CP violation of hadrons containing b quarks.

2.2 Physics at LHC

2.2.1 The standard model and Higgs mechanism

The standard model (SM) of particle physics is based on three interactions. These interactions are strong interaction, weak interaction and electromagnetic interaction and are described by an unified framework of the gauge theory. There are six types of quarks and leptons and three types of gauge bosons; photon, gluons and W/Z weak bosons, which mediate the electromagnetic, strong and weak force, respectively.

To keep a gauge theory re-normalizable, it is requested that all masses of particles are zero. The mass of photons and gluons are zero but weak bosons have quite big masses. (W boson has a mass of 80.4 GeV and Z boson is 91.2 GeV). The electroweak theory [6] solved this problem by the idea of the spontaneous symmetry breaking (SSB) now known as the "Higgs Mechanism." To invoke the SSB, the Higgs field is introduced and fermions are interacting with the field strongly with the Yukawa interaction. After the SSB, it is predicted that there is at least one massive scale boson which is called a Higgs boson (H). A very rough estimate of the Higgs mass could be based simply on dimension analysis.

$$M_H \approx \frac{1}{\sqrt{\sqrt{2}}} G_F = 246\ GeV,$$

here $G_F \sim 10^{-5}/m_p^2$ is the Fermi constant of the weak interaction. We expect that Higgs mass might be near this scale. Experimentally, we now know Higgs mass is not lighter than 114.4 GeV from LEP experiments. In LHC we can search for the Higgs particle in the wider range from below the LEP limit to ∼1 TeV.

2.2.2 Higgs production and decay mode

There are four major Higgs production processes at the LHC energy. Figure 2.2 shows examples of these four Feynman graphs.

- gluon-gluon Fusion ($gg \rightarrow H$)
  Higgs is produced from a fusion of two gluons. Although gluons do not directly couple to Higgs, the process occurs via the internal quark loops. This process has biggest cross sections at LHC energy.

- WZ Fusion ($qq \rightarrow qqH$)

  Higgs is produced from a fusion of two vector bosons ($W^{\pm}$ or Z^0) which are emitted from quarks. The two scattered quarks tend to be emitted in the forward direction with relatively high have transverse momenta (p_T).

- Higgs-Strahlung ($q\bar{q} \rightarrow (W/Z)H$)

  This is popular process at particle-antiparticle collider such as Tevatron but is minor process at LHC.

- tt Fusion ($gg \rightarrow t\bar{t}H$)

  From pair of two t quarks Higgs is produced. The cross section of this process is small, but measurable when Higgs is light. The process is important for measurement of the ttH coupling.

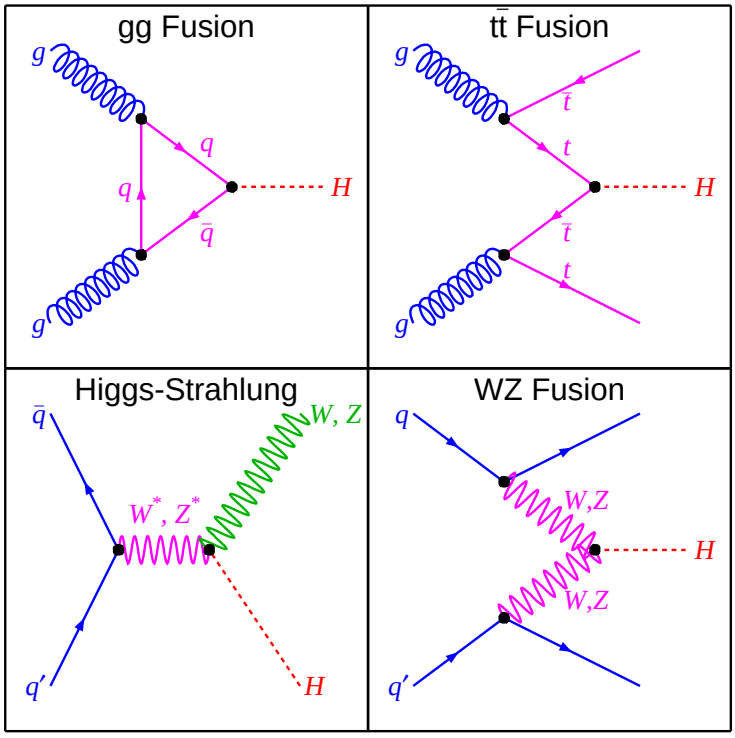

Figure 2.2: Higgs Production Process [7]

2.2.3 Decay Mode

The coupling constant of Higgs to fermions is proportional to the fermion mass. Therefore Higgs dominantly decays to the heaviest fermion which is kinematically reachable. The coupling to the weak bosons are generally bigger then fermion. As shown in Figure 2.3, main decay modes depends on the mass of Higgs. If Higgs mass is heavier than twice of the weak boson mass, these two decay mode are dominant;

$$H \to W^+W^-, H \to Z^0Z^0.$$

On the other hand, if Higgs mass is lighter than twice of weak boson mass, following decay modes are dominant.

$$H \to b\bar{b}, H \to \tau^+\tau^-.$$

Since γ is easy for measuring, $H \to \gamma^+\gamma^-$ is also important decay mode. In the most of the case, muon is good signature for the Higgs search. Muons from the W/Z decays are a good signature for Higgs and/or top productions. When Higgs decays into $b\bar{b}$, muons from leptonic decays of b quark might be used, too.

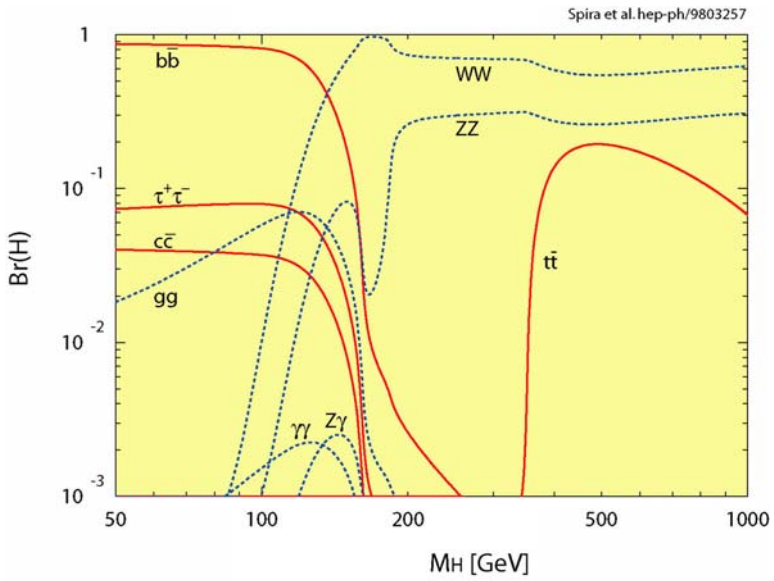

Figure 2.3: Higgs Decay Branching Ratios [8]

2.2.4 New physics at LHC

Although Higgs is the last missing piece of the SM, there are still several unexplained things in the SM. For example, mass of Higgs boson diverges at the loop level due to the self-coupling of Higgs boson. If there are some particles which behave same as SM particles but only differ in spin, this divergence of Higgs mass is canceled. Such particles are predicted in the supersymmetric (SUSY) models. And these SUSY particles are expected to have mass of order 1 TeV. If so, they are seen at LHC.

Some more new physics (ex. extra-dimension) are also expected to be discovered.

2.3 ATLAS detector

The overall ATLAS detector layout is shown in Figure 2.4. It consists of several systems; magnets, inner detectors, calorimeters and muon spectrometers. From the innermost, inner detectors are equipped around the beam pipe. Inner detectors measure tracks of particles with a high granularity. Outside of the inner detector, a solenoid magnet is aligned on the beam axis and provide axial magnetic field for the inner detectors. Outside the solenoid, calorimeters which measures energy of particles are equipped. At the outermost, muon spectrometers with toroidal magnets are equipped. The size of the ATLAS detector are approximately 25 m in height and 44 m in length. The over all weight of the detector is about 7,000 tonnes.

2.3.1 Coordinate system

The ATLAS coordinate system is a right-handed Cartesian system. The nominal interaction point is defined as the origin of the coordinate system. The beam direction defines the z-axis. The positive x-axis is defined as pointing from the interaction point to the center of the LHC ring and the y-axis is defined as pointing upwards. The ATLAS detector can be geometrically divided into two a barrel and two end-caps. Each side of end-cap are called side-A or side-C. The side-A is the positive z side and side-C is the negative z side. The azimuthal angle ϕ is measured as usual around the z axis, and polar angle θ is the angle from z axis. The pseudo-rapidity (η) is defined as

$$\eta = -\ln \tan\left(\frac{\theta}{2}\right).$$

To explain the distance from beam line R ($R = \sqrt{x^2 + y^2}$) is used.

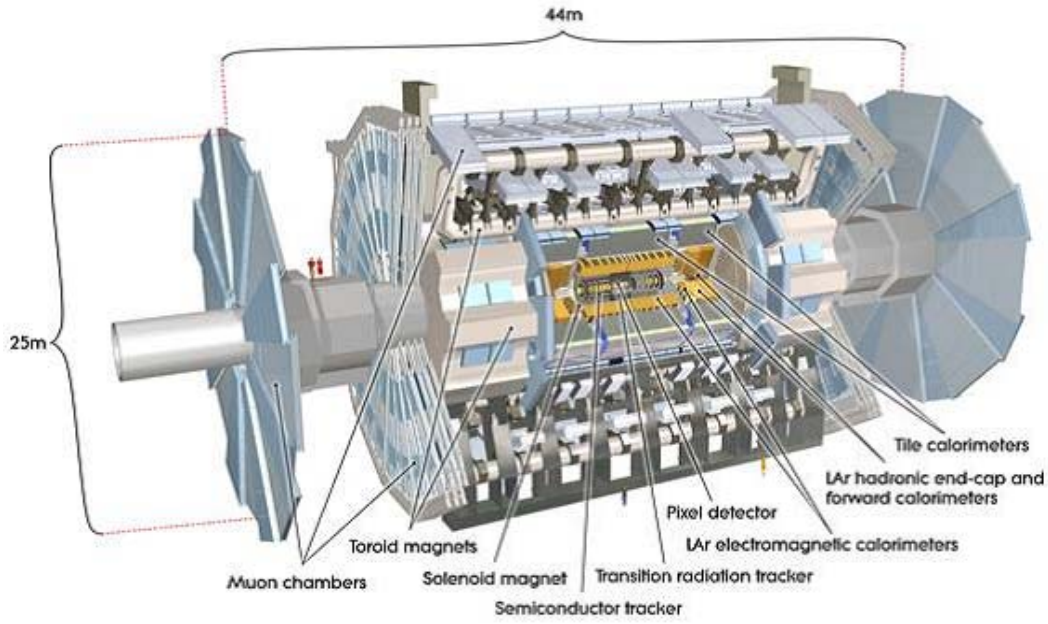

Figure 2.4: Over all ATLAS detector

2.3.2 Magnets

There are two types of magnet used in the ATLAS detector; a solenoid magnet and toroidal magnets.

Layout of the magnet system is shown in Figure 2.5 (a).

Solenoid magnet [2]

A superconducting solenoid magnet is located outside of the inner detectors and inside of the calorimeters. The inner and outer diameters of solenoid are 2.46 m and 2.56 m, and its z-axial length is 5.8 m. It is designed to provide 2 T magnetic field. To keep a better calorimeter performance, the material thickness in front of the calorimeter should be as low as possible. For this reason, the solenoid and calorimeter share a common vacuum vessel. The solenoid itself is designed to be very thin.

Toroid magnet

The toroidal magnet system consists of a barrel part and two end-cap parts. A barrel toroid and two end-cap toroid provide magnetic field of approximately 0.5 T and 1 T for muon detectors at the barrel and end-cap respectively.

Each barrel toroid and end-cap toroid has eight superconducting coils arranged in axial symmetry. Two end-cap toroids are inserted to each end of the barrel toroid. Figure 2.5 (b) shows field on x-y plane at z = 11 m where both the barrel and end-cap toroid are visible. The red rectangulars indicate the coils of the barrel toroid and green rectangulars do coils of the end-cap toroid. The barrel and end-cap magnetic field interfere each other so that there are some regions where the field is very weak.

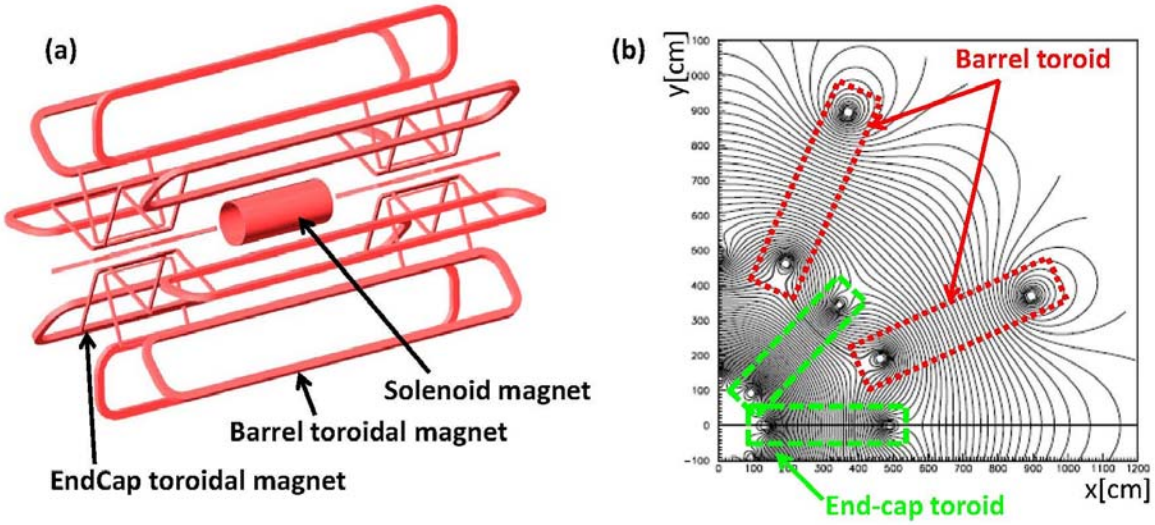

Figure 2.5: (a) Layout of the magnets (b) Intensity of magnetic field on x-y plane at z = 11 m

2.3.3 Inner Detector

The layout of the inner detector is shown in Figure 2.6. It consists of pixel detectors, Semiconductor Trackers (SCT) and Transition Radiation Trackers (TRT). SCT and TRT are divided into two end-cap parts and a barrel part. The pixel detectors are located inside the barrel SCT.

These detectors are located in the magnetic field produced by the solenoid magnet

and are to measure charged tracks precisely to determine their momenta and the vertex point. So these detectors have a good position resolution with fine granularity.

The pixel detector

The highest granularity is achieved around vertex region using the silicon pixel detector. All pixel sensors are identical. A pixel has a rectangular shape with a size of 50×400 μm^2. The intrinsic resolution are 10 μm for the Rϕ direction and 115 μm for the z direction.

The Semiconductor Tracker (SCT)

The SCT consists of silicon strip detectors with binary readout. Sensors are arranged to form four coaxial cylindrical layers at the barrel and nine disk layers at the each end-cap. At the barrel, two sensors are combined with 40 mrad degree tilting angle to allow the two dimensional position determination. The pitch of the strip is 80 μm. At the end-cap, modules are trapezoidal shape with strips running radially and set of stereo strip at an angle of 40 mrad. The intrinsic resolution at the barrel are 17 μm (Rϕ) and 580 μm (z), and at end-cap disk are 17 μm (Rϕ) and 580 μm (R).

The Transition Radiation Tracker (TRT)

The purpose of the TRT is two folds; to track charged particles at the outermost radius in the inner detector and to detect the transition radiation to identify electrons. The TRT consists of polymide drift (straw) tubes of 4 mm diameter. The gas mixture of Xe, CO_2, O_2 is used. The TRT is also divided into a barrel region and two end-cap regions. At the barrel, tubes are in parallel to the beam axis and are 144 cm long. They provide only Rϕ information, with an intrinsic resolution of 130 μm. At the end-cap region, tubes are arranged radially in wheels and are 37 cm long.

2.3.4 Calorimeter

Figure 2.7 (a) shows overall of calorimeter layout. The calorimeter consists of a barrel, two end-caps, and two forward parts. Here, forward part is closer region to the beam line than the end-cap. Each calorimeter is longitudinally divided into electromagnetic (EM) calorimeter and hadronic calorimeter. The EM calorimeter is the front part and is

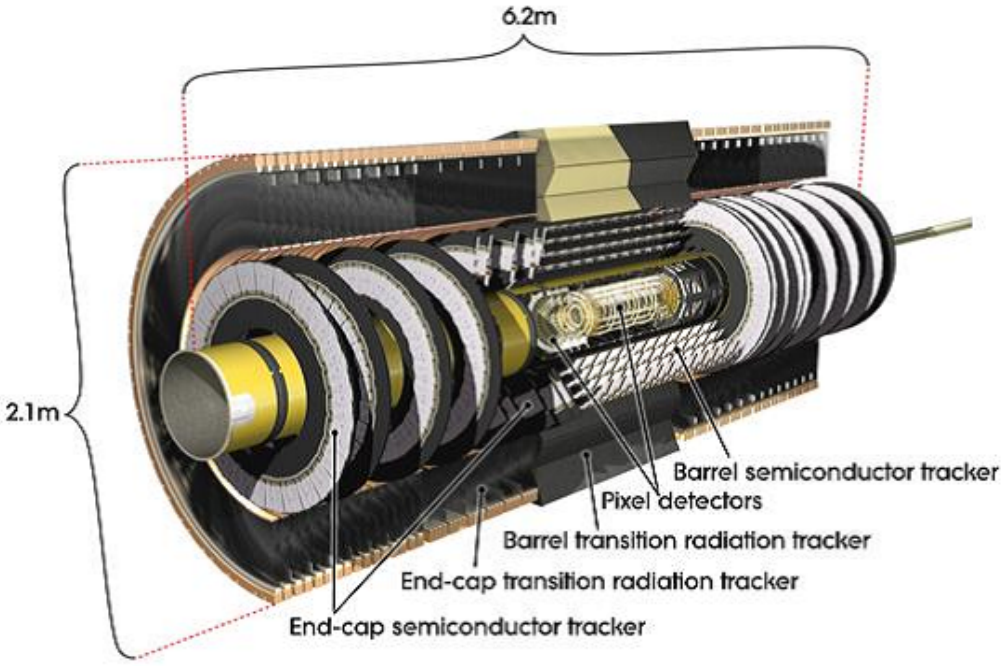

Figure 2.6: Layout of inner detector

used for measuring electron and photon energies and positions. The hadronic calorimeter which surrounds the EM calorimeter is used for measuring energy leaking from the EM calorimeter. Since hadronic showers develop less rapidly than electrons or photons, the hadronic calorimeter is much thicker than the electromagnetic calorimeter.

The electromagnetic calorimeter

The EM barrel and end-cap calorimeter is lead-LAr detector with accordion-shaped kapton electrodes and lead absorber plates. Figure 2.7 (b) shows this accordion-shaped kapton electrodes. The EM calorimeter has a full coverage in ϕ without any cracks. The lead thickness in the absorber plates has been optimized as a function of η in terms of the energy resolution. The EM forward calorimeter has different structure from others. Copper plates are stacked one behind the other and are drilled several holes in them through which the electrode structures are inserted. An electrode consists of coaxial copper rod and copper tube separated by a radiation-hard plastic fiber wound around the rod. LAr is filled between the rod and the tube.

Hadronic calorimeter

The hadronic calorimeters have different structures in the each parts. The hadronic barrel calorimeter is sampling calorimeter using steel as the absorber and plastic scintillating tiles as the active material. The hadronic end-cap calorimeter is copper-LAr sampling calorimeter with flat plate design which is located directly behind the end-cap electromagnetic calorimeter and sharing the same LAr cryostats. The hadronic forward calorimeter is similar to the EM forward calorimeter, except for the use of tungsten rods instead of copper rods and for the use of tungsten slugs as absorber instead of copper plates.

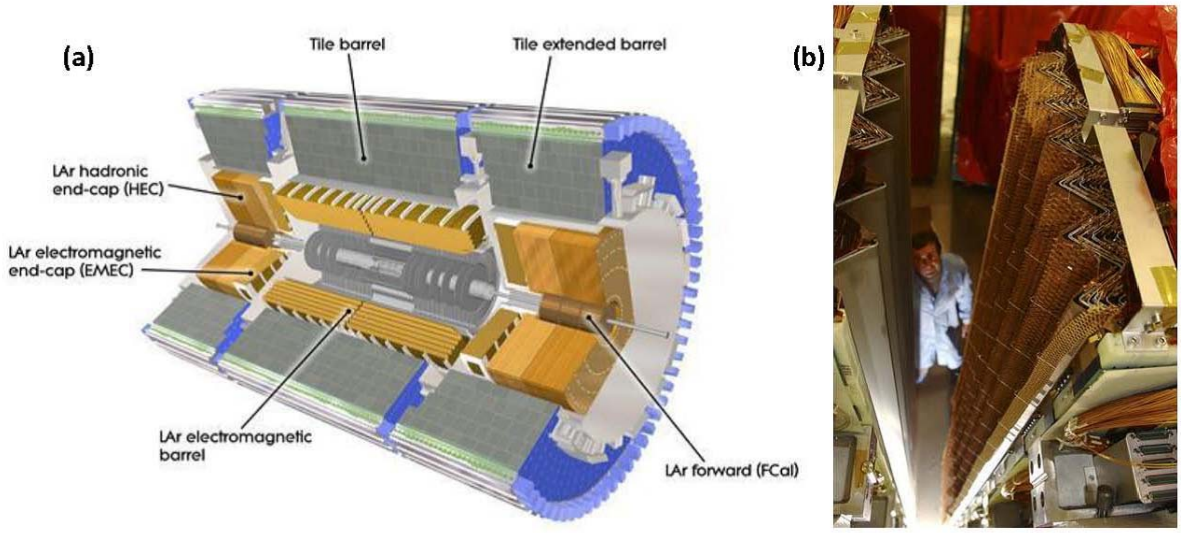

Figure 2.7: (a) Layout of calorimeter (b) Accordion geometry of electromagnetic calorimeter

2.3.5 Muon spectrometer

Muon particles pass through calorimeters and bended by magnetic field provided by toroidal magnets. The muon spectrometers detect the trajectory and measure the muon momentum.

The muon spectrometer is also divided into a barrel part and two end-cap parts. The muon spectrometer consists of several detectors, Thin Gap Chambers (TGC), Resistive Plate Chambers (RPC), Cathode Strip Chambers (CSC) and Monitored Drift Tubes

(MDT). RPC is equipped at the barrel, TGC is equipped at the end-cap, CSC is equipped at forward region at the end-cap and MDT is equipped at both end-cap and barrel. RPC and TGC are used for triggering and MDT and CSC are used for precision measurement.

Figure 2.8 shows layout of muon spectrometers. In Figure 2.8, pink colored object at the end-cap shows TGC, light blue colored at the end-cap and light green at barrel shows MDT, yellow colored object at the end-cap shows CSC and white box beside MDT at barrel shows RPC. The coverage of each detectors are listed in table 2.3.5.

At both barrel and end-cap, there are three layers; inner layer, middle layer and outer layer. At the barrel, MDT is equipped at each layers and RPC is equipped at middle and outer layer. At the end-cap region, MDT is also equipped at each layers, TGC is equipped at middle layer and CSC is equipped at forward region of inner layer. More detailed layout is described in Chapter 3.

In this section, structure of each types of detectors .

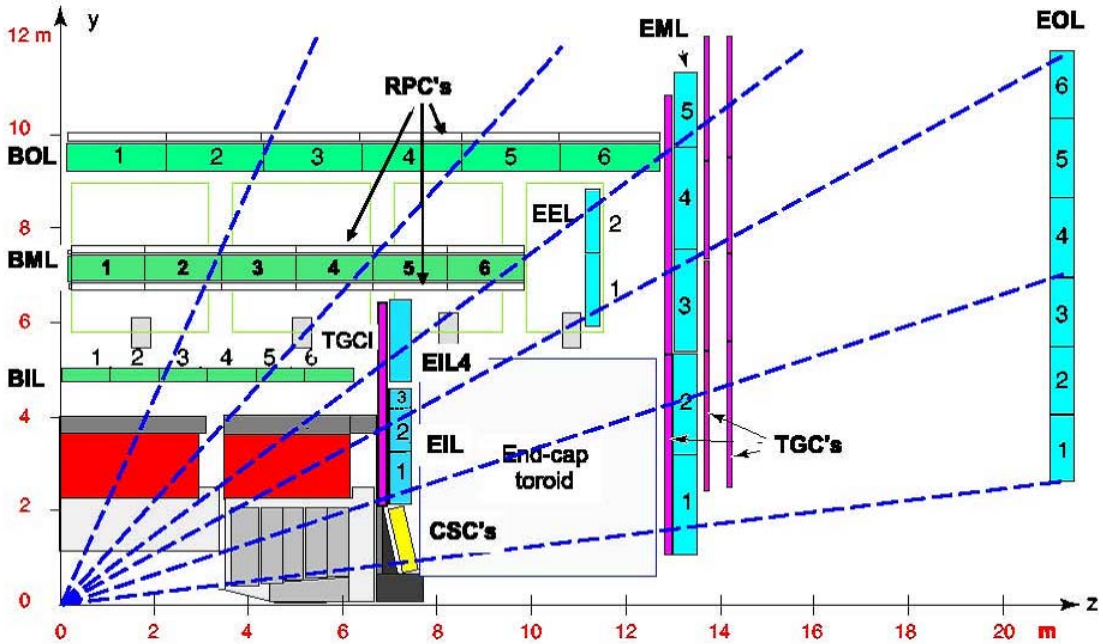

Figure 2.8: Layout of muon spectrometers

RPC	$\|\eta\| < 1.05$
TGC	$1.05 < \|\eta\| < 2.7(2.4\ for\ triggering)$
MDT	$\|\eta\| < 2.7(innermost\ layer : \|\eta\| < 2.0)$
CSC	$2.0 < \|\eta\| < 2.7(Only\ inner\ layer\ at\ the\ endcap)$

Table 2.2: Coverage of muon chambers

RPC

RPC is gaseous resistive parallel plate chamber. Two resistive plate which are made of phenolic-melaminic plastic laminate are kept parallel to each other at distance of 2 mm supported by insulating spacers. The electric field between plates is about 4.9 kV/mm which allows avalanches to form along the ionizing tracks towards the anode. The signal is read out via capacitive coupling of metallic strips which are mounted on the outer face of the resistive plates.

The gas used is a mixture of $C_2H_2F_4/I_{SO}-C_4H_{10}/SF_6$ (94.7/5/0.3). Normal operating voltage is 9.8 kV. Position resolution is 1 cm.

TGC

TGC is a type of Multi Wire Proportional Chamber (MWPC) which consists of anode wires, cathode planes, strip planes, shields and honey comb support structures. The gap between the anode wire and cathode plane (1.4 mm) is smaller than the distance between the anode wires (1.8 mm). From this fact the name stems.

A highly quenching gas mixture of CO_2 and n-C_5H_{12} (n-pentane) (55/45) is used. The high electric field around the wires and the small distance between the wires result in a very good time resolution. (Signal arrive with 99 % probability inside a time window of 25 ns.) Figure 2.9 shows end-cap wheel which consists of number of TGC.

MDT

MDT is a drift tube which diameter is about 30 mm. The electrons from ionization are collected at the central tungsten-rhenium wire with a diameter of 50 μm, at a potential of 3080 V. The wire is held at the end of tube by a cylindrical end-plug which guarantees the concentricity of the wire with respect to the tube with an accuracy of $\sigma < 10\mu m$. The

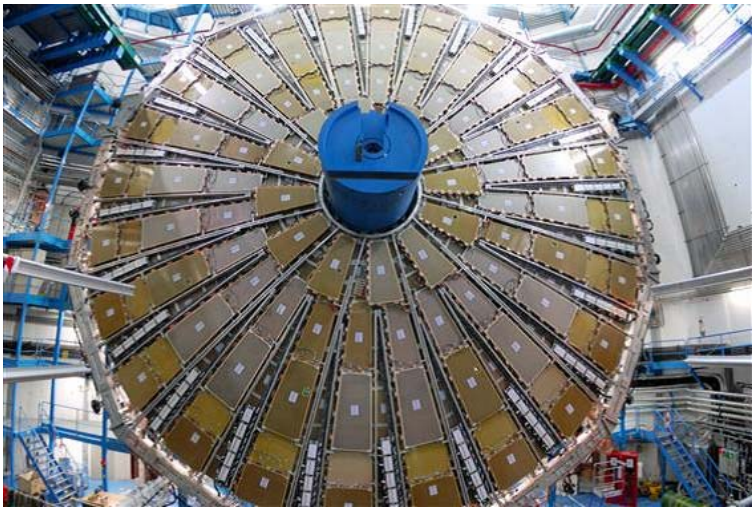

Figure 2.9: One side of end-cap wheel consists of number of TGCs

gas used is Ar/CO_2 (93/7). The maximum drift time from the wall to wire is about 700 ns and the average resolution per tube is $\sim 80\mu m$.

Tubes are combined in a rectangular module at the barrel and trapezoidal module at the end-cap. For the inner layer station, four modules are layered together and three layers for two middle and outer layer stations. Figure 2.10 shows a trapezoidal module. The direction of tubes is tangential to circles around beam line. Thus MDT can measure the hit position with higher accuracy than RPC and TGC in η direction.

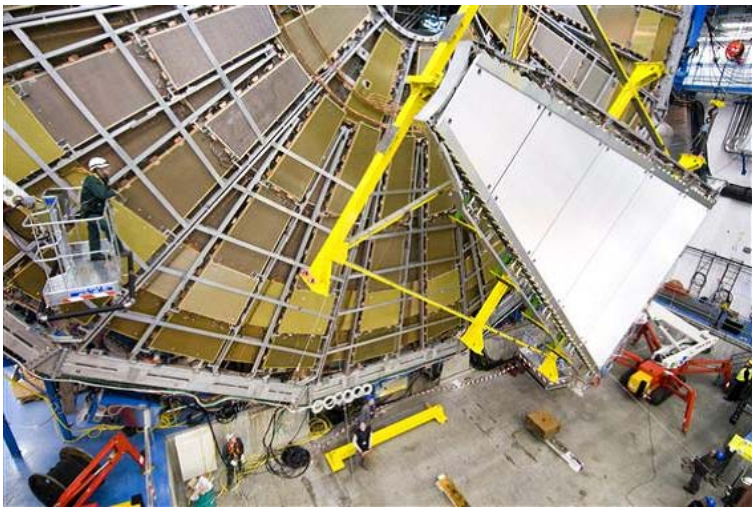

Figure 2.10: A trapezoidal MDT module at the end-cap

CSC

CSC is the type of MWPC consists of wires and two cathode strip layers. The wires are held in the radial direction and one cathode strips are perpendicular to the wires and the other cathode strips are parallel to the wires. The gas used is Ar/CO_2 (80/20). Position resolution is 60 μm per CSC plane.

Chapter 3

Muon Trigger System

To select interesting events among a large number of events, well optimized trigger system is required. In this chapter, general ATLAS trigger system is described at first. Second detailed muon system are explained, with emphases on the trigger aspect. Then about the problem at magnetic field in end-cap is described.

3.1 ATLAS trigger scheme

To achieve the rate reduction, ATLAS has adopted a three-level trigger system; Level1 (L1) trigger, Level2 (L2) trigger and Event Filter (EF). The L1 trigger is based on custom-made electronics. The L2 trigger and EF are entirely software based.

Figure 3.1 shows a schematic view of the ATLAS trigger system. The L1 trigger searches for signature of high p_T (transverse momentum) muons, electrons, photons, jets and τ leptons. Its selection is based on information from subset of detectors. Events passing the L1 trigger selection are transferred to local buffers and wait for the L2 decision. Based on the L1 trigger, Region-of-Interest (RoI) is determined in the $\eta \times \phi$ space. RoI is the region where the L1 finds the triggered object.

L2 trigger is seeded by the RoI information; *i.e.* the readout data of the specified regions are collected to use the trigger decision. The L2 trigger can use, at full granularity and precision, all the available detector data within the RoI. With the RoI mechanism, amount of data to transfer and to analyze can be reduced hence the time for trigger decision is shortened. The events selected by the L2 trigger are transferred for the event-building, and subsequently fed to the EF for the final selection.

Events selected by the EF are moved to mass storage system at the CERN computer center.

The maximum L1 trigger accept rate is set to 75 kHz (upgradeable to 100 kHz), and the L1 trigger decision is to reach the to front-end electronics within 2.5 μs after the bunch crossing. The L2 trigger reduces the trigger rate below 3.5 kHz with latency of 40ms. The EF reduces to trigger rate below 200 Hz, with an average latency of four seconds.

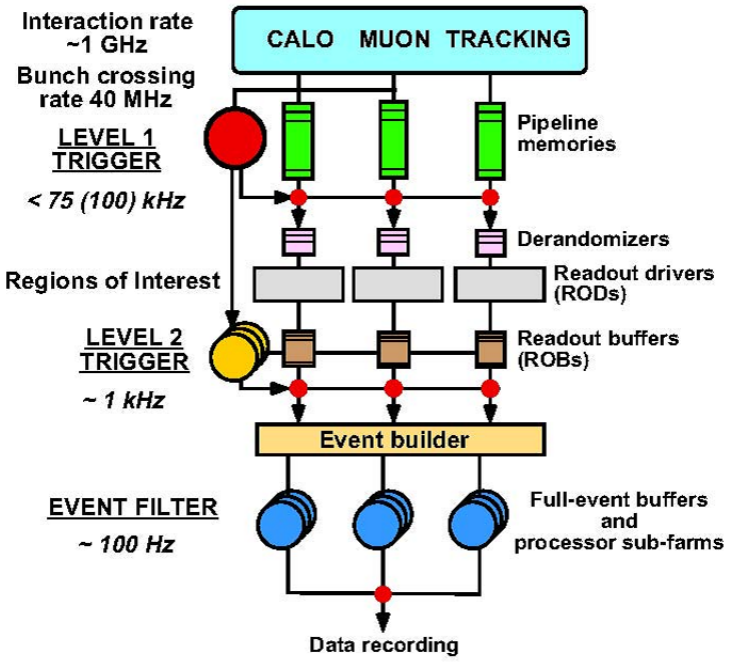

Figure 3.1: Trigger scheme [9]

3.2 Muon Detector layout

As described in Chapter 2, muon detectors are divided in to a barrel part and two end-cap parts. In this section, detector layout is described for each parts.

3.2.1 The barrel part

The barrel muon system is installed to cover the whole 2π region in the ϕ direction. With the presence of the barrel toroid, this is not trivial. There are two types of layout, small and large sectors. As seen in Figure 3.2, the small sectors cover the ϕ regions with

toroidal magnet coils, and the large sectors covers the region between coils. At the bottom part of ATLAS detector, muon system is installed between the support structure (feet). Therefore, these small and large sectors are special.

Each sector has three layer structure. Each layer are located as shown in Figure 3.2. At the inner layer, two MDT layers are equipped. At the middle layer two RPC layers are equipped sandwiching two MDT layers. At the outer layer, one RPC layer and two MDT layers are equipped. Since each RPC layer is made of 2 sets of RPCs, one layer gives two hits in both η and ϕ directions. At the middle layer, a 3-out-of-4 coincidence in both η and ϕ projection is required for the L1 trigger. At the outer layer, 1-out-of-2 hit is required. By this coincidence, fake tracks from noise hits are eliminated.

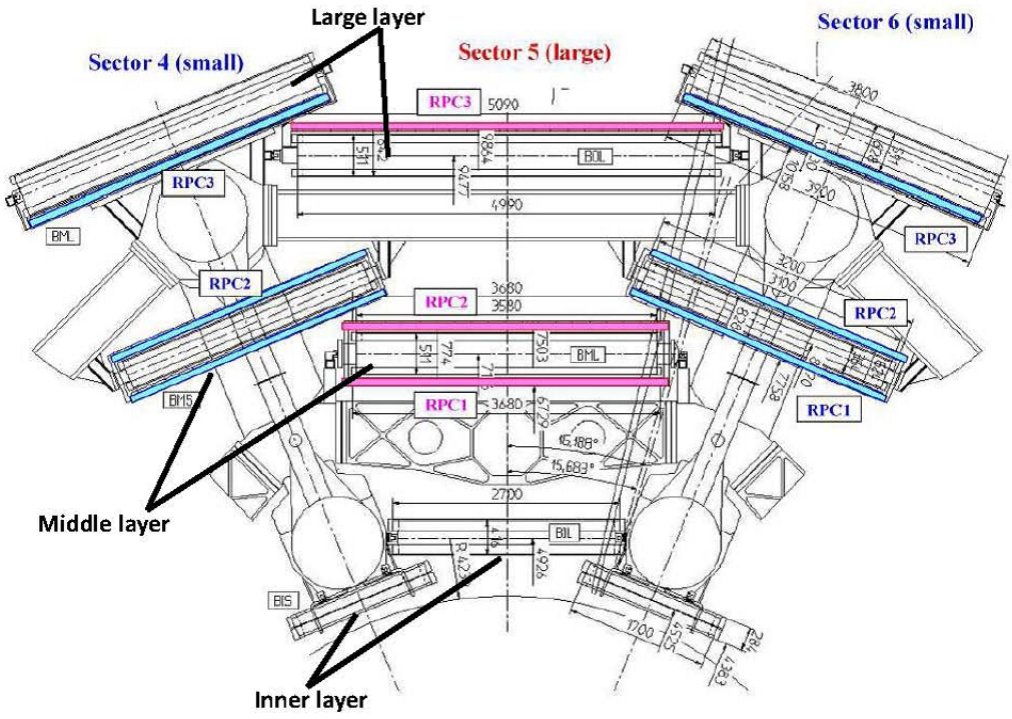

Figure 3.2: Layout of barrel muon system. RPCs are indicated in blue (small sector) and red (large sector). The circles are the cross section of barrel toroidal coils.

3.2.2 The end-cap part

At the end-cap, TGC, MDT and CSC are equipped. At the inner layer, two MDT chamber layers and one CSC plane are equipped beside two TGC chamber layers. At the middle

layer, three and four TGC chamber layers are equipped sandwiching two MDT chamber layers. At the outer layer, two MDT chamber layers are equipped.

Each wheels are divided into eight trapezoidal lumps which are called "octant". The octant consists of several sectors of MDT or TGC. Figure 3.4 shows the shapes of octant of TGC. MDT is also divided into small and large sectors same as the barrel. The octant of MDT consists of one small sector and one large sector.

There are two types of TGC module, one is doublet module and the other one is triplet module. Figure 3.3 shows the cross section of doublet and triplet modules. The doublet module consists of two gas chamber layers, and the triplet module has three layers. The doublet module has two cathode strips and two wire planes, and the triplet module has two cathode strips and three wire planes. The cathode is marked as "Cu strips" in this figure. The cathode strip uses to measure the azimuthal position and radial coordinate is determined with the anode read out. At the inner layer, one doublet module is equipped and at the middle layer a triplet module and two doublet module are equipped.

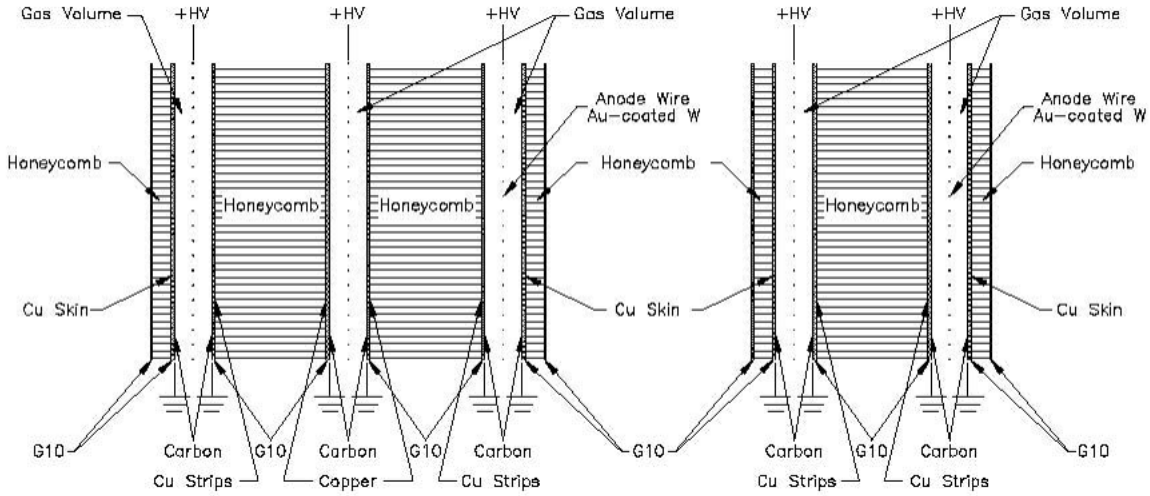

Figure 3.3: Cross section of TGC: (Left) The triplet module (Right)The doublet module [2]

3.3 Level1 muon trigger system

The L1 muon trigger aims to search for patterns of hits consistent with high-p_T muons originating from the interaction point. L1 end-cap muon trigger use the only middle layer.

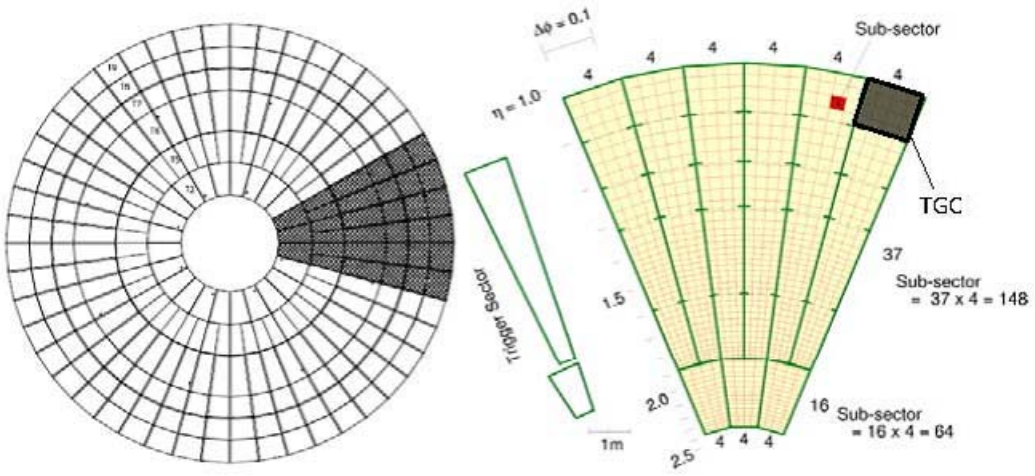

Figure 3.4: Left: Octant at wheel Right: Alignment of TGC in octant [9]

From triplet module, 2-out-of-3 coincidence is formed while 3-out-of-4 is made from the signals of two doublet.

Using δR and $\delta\phi$, the L1 muon trigger decision is made. δR is difference of R in the middle layer, and $\delta\phi$ is difference of ϕ in the middle layer.The muon trigger has six independently-programmable pT thresholds.

The over all L1 accept decision is made by Central Trigger Processor (CTP), which combines the muon trigger and calorimeter trigger.

3.4 Level2 muon trigger system

There are three steps in the L2 trigger. The algorithm used in first step is named "muFast" which only uses information from muon detectors, and reconstruct p_T. The algorithm used in the second step is named "muComb" which uses both information from inner detector and muon detector (actually out put of muFast is used). The algorithm used in the third step is named muIso which check the isolation criteria using information of calorimeter. L2 trigger is seeded by RoI which is made from the L1 trigger.

In this section, description of muComb and muIso are written. The description about muFast is written in Chapter 4.

- **muComb**

  MuComb reconstruct tracks at inner detector around the muon track which is found

by muFast and match them at the surface called "matching surface." Then the distance between the inner track and muon track is calculated. The distance of two point is described in ΔR (Δ R = $\sqrt{\Delta\eta^2 + \Delta\phi^2}$; here $\Delta\eta$ means difference between two point in η direction and $\Delta\phi$ means difference between two points in ϕ direction.) If the value of ΔR is over a threshold value, then muComb cut that trigger candidate. Since the magnetic field is not uniform and particles pass through the different material at each region and make different curve, the matching surface is divided into small segments, and values of threshold differs at each segments. Muon p_T is calculated using inner detector.

- **muIso**
  MuIso find isolated muon which is not produced from jets. For the isolating the information of calorimeters are used.

3.5 Muon trigger in Event Filter

In the EF, precision position on the detector is used and make trigger decision. "MOORE" and "MuId" are used for the purpose of muon reconstruction and identification[10].

Chapter 4

muFast

Around seeded RoI information from the L1 muon trigger, muFast seeks a track in the muon detector. First muFast finds a muon track segment at the each inner, middle and outer layer. From a track segment, muFast determines a "super-point" which is a set of position in the layer and the track direction. MuFast then finds a track using these super-points, and reconstructs p_T.

In the L2 trigger, the better p_T measurement is possible than in the L1 trigger, because more precise position from MDT is usable. Since the MDT provides only η position, the information of TGC or RPC are used for the ϕ direction.

There are two algorithms in muFast. One is for the barrel part and the other is for the end-cap part. Each algorithms are described in this section.

4.1 Algorithm at barrel

Since the magnetic field provided by the barrel toroid is nearly perpendicular to the particles emitted from the interaction point, momentum of charged particles is described in $p_T[GeV/c] = 0.3B[T]R[m]\sin\theta$. Here, B is intensity of magnetic field provided barrel toroid magnet, θ is the direction of the particle at the interaction point.

In the algorithm of barrel part, muFast uses this formula to reconstruct transverse momentum. If there are three measured points, it is possible to calculate the radius (R). If only two points, the nominal interaction point is also used for extract the radius. Using this radius, muFast calculates transverse momentum p_T using the formula

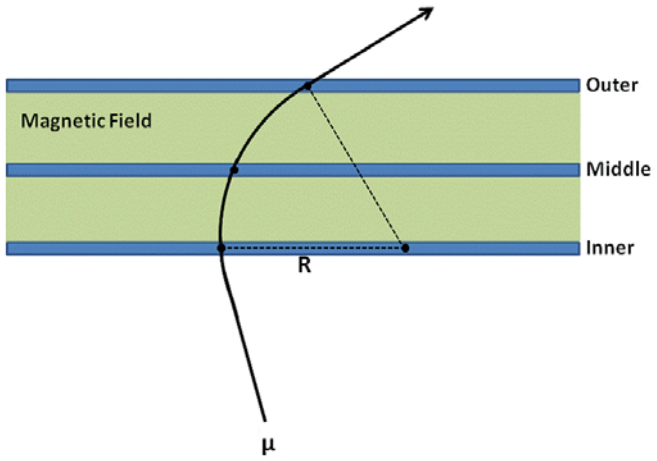

Figure 4.1: Radius

$$p_T = AR + B. \tag{4.1}$$

Here A and B are coefficients. If the field is uniform and there is no ϕ component in the particle momentum, from (4.1), $A = 0.3B\sin\theta$ and $B = 0$.

Because magnetic field is not uniform, the coefficients vary for η and ϕ. MuFast divides barrel part into small regions in η direction and ϕ direction. This segmented region is called "bin", and these coefficients are determined for each bins. These coefficients are determined in advance by using the single muon Monte Carlro events with $p_T = 6$ and 40 GeV. The coefficients are stored in a reference table which is called "look up table" (LUT). Thus, muFast calculates transverse momentum with a simple linear function $p_T = A_{ij}R + B_{ij}$ (i,j are bin number), and saves the time for calculation. Here, the coefficients are set with the unit of GeV for p_T and cm for R.

MuFast divides each sectors into 30×30 bins for η and ϕ direction. For small, large, small special and large special sectors, two patterns of tables are prepared, one is for positive charge and the other is for negative charge. To summarize, there are eight LUTs.

Figure 4.2 shows coefficients for positive charge, and Figure 4.3 shows coefficients for negative charge. In both Figure 4.2 and Figure 4.3, histograms in the upper stand shows value of coefficient A in (4.1) and histograms in the lower stand shows coefficient B in (4.1). From left side, histograms of coefficient at the large sector, the large special sector, the small sector and small special sector are shown. The abscissa axis shows η direction

and longitudinal axis shows ϕ direction. In each histograms, the cell which is not colored means the values are out of color range.

If we take the normal magnetic field of 0.5 T, $A_{ij} = 0.0015$ at $\eta = 0$ and $A_{ij} = 0.0011$ at $\eta = 0.8$ (η bin = 25). The figure indicates this trend but also some deviation as a function of ϕ. This is from the inhomogeneity. The strange distribution of the small special sector is a reflection that the region is not well covered with the muon detectors because of the support structure. The coefficient for positive and negative particles are almost identical when the sign of η is flipped, as expected.

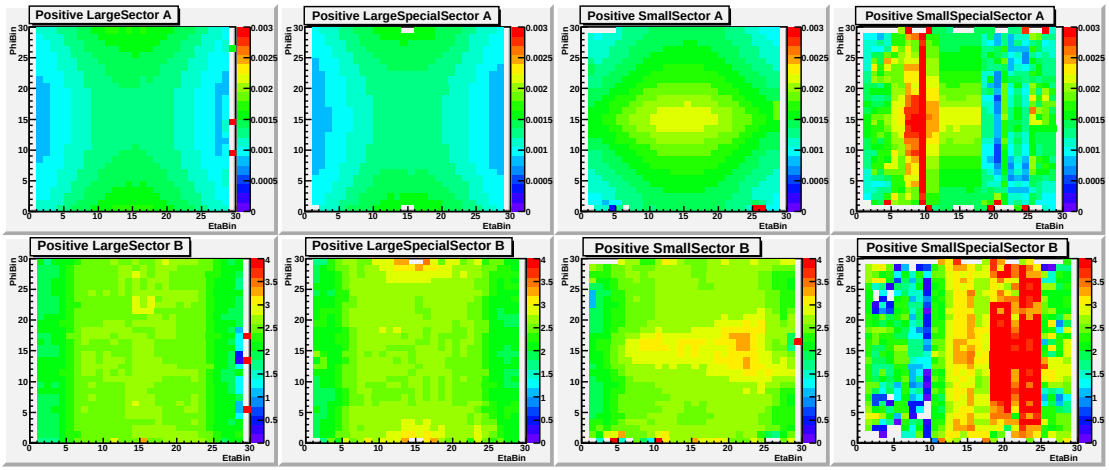

Figure 4.2: Coefficients for positive charge at the barrel

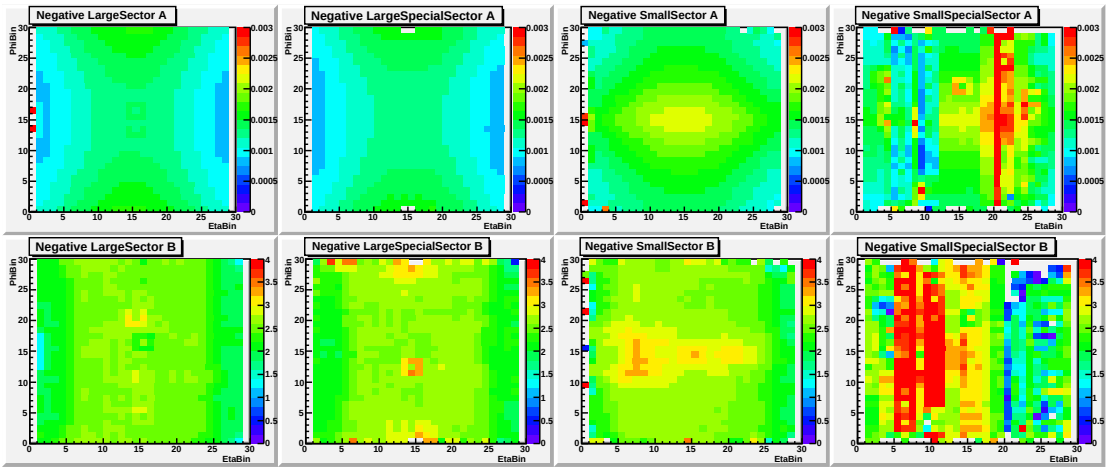

Figure 4.3: Coefficients for negative charge at the barrel

4.2 Algorithm at end-cap

In the end-cap part, muFast uses an angle which is named α instead of the radius. This α is defined as shown in Figure 4.4. There are two lines in Figure 4.4, one is the line connecting the point in the middle layer and the nominal interaction point. *i.e.* (z,R) = (0,0). The other line is the direction of the super-point of the middle layer, or if there is a super-point at the outer layer, the line to connect the two super-points. The angle α is defined as angle between the two lines. Since L1 trigger is fired based on hits in the middle layer only, The α can be measured all events passed L1 trigger. This is the advantage of the usage of α since loss of the efficiency is the minimum. The relation between α and muon momentum is rather complicated. But in muFast it is parameterized with a following linear formula,

$$\frac{1}{p_T} = A_{ij}\alpha + B_{ij}, \tag{4.2}$$

where A_{ij} and B_{ij} are coefficients again for small η bins. These coefficients are determined for each bins. As described in section 3.2, the end-cap toroid has 8-fold symmetry so that the same coefficients are used for all octant. There is a mirror symmetry in each octant in ϕ, so that muFast divides the whole range of the octant into 30 bins in η, and half range of octant into 12 bins in ϕ. In the standard muFast the sign of α is ignored, so that the same LUT is used for positive and negative particles. In summary, α is used for the entire region. Figure 4.5 shows coefficients (A,B) in equation (4.2). The left histogram shows coefficient A_{ij} in and the right histogram shows coefficient B_{ij}. Since the integrated magnetic field is weak at the specific region[1] the values of coefficient A is higher in this region than others.

4.3 Magnetic field at the end-cap

As described in 2.3.1, the magnetic field at the end-cap is highly nonuniform. Figure 4.6 (a) shows field map on z-R plane at $\phi = \pi/8$. At the region where z is 9 m$\sim$13 m and R is $\sim$4.5 m, the magnetic field becomes weak. And distribution of line of magnetic force on

[1]Figure 4.11 shows number of L1 triggered events at each bins using $p_T = 4$ GeV samples. Even though threshold is set to 6 GeV, 4 GeV muons are triggered at region of $7 < \eta\ bin < 9,\ \phi = 0\ and\ 11 < \eta < 14,\ 9 < \phi < 11$. The intensity of magnetic field is weak here and p_T of muons are overestimated.

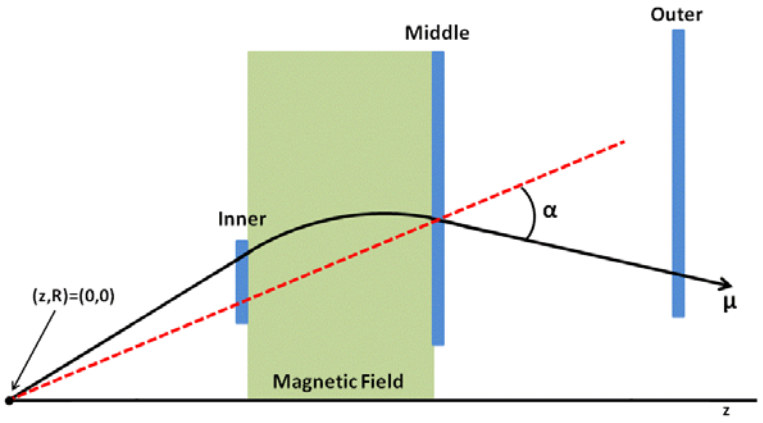

Figure 4.4: Definition of α

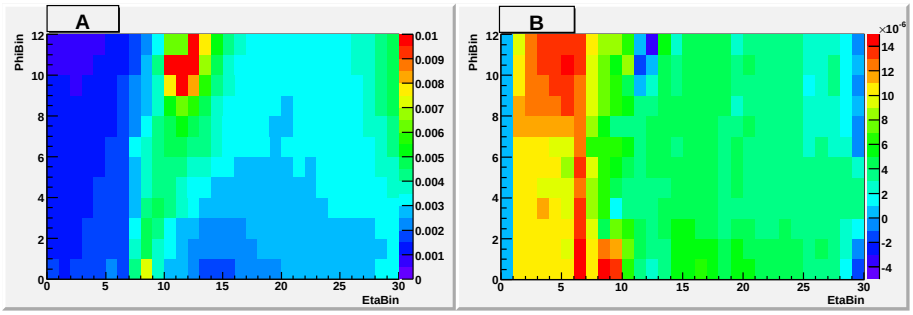

Figure 4.5: Coefficients at the end-cap part

x-y plane at z=11 m is shown at Figure 4.6 (b). Around the coils which locate at R=500 cm ($R^2 = x^2 + y^2$), there are a wider space than the others between lines, and this means the intensity of magnetic field is weak here. This is due to an interface between barrel and end-cap toroids.

Charged particles which pass through this region feel less integrated magnetic field so that they do not curve so much. A histogram (a) in Figure 4.7 shows how different the measured η at the end-cap middle layer point, compared with the initial η at the interaction point. This histogram is plotted using simulated single muon samples[2] whose transverse momentum (p_T) is 4GeV. X axis represents position of η at the end-cap middle layer and Y axis represents the difference as mentioned. At the region of $1.4 < \eta < 1.6$, $|\Delta\eta|$ becomes smaller and almost zero. This means muons in the region are bended less.

[2]Simulated single muon sample is produced using ATLAS simulating software. Single muons are generated flat in η and ϕ.

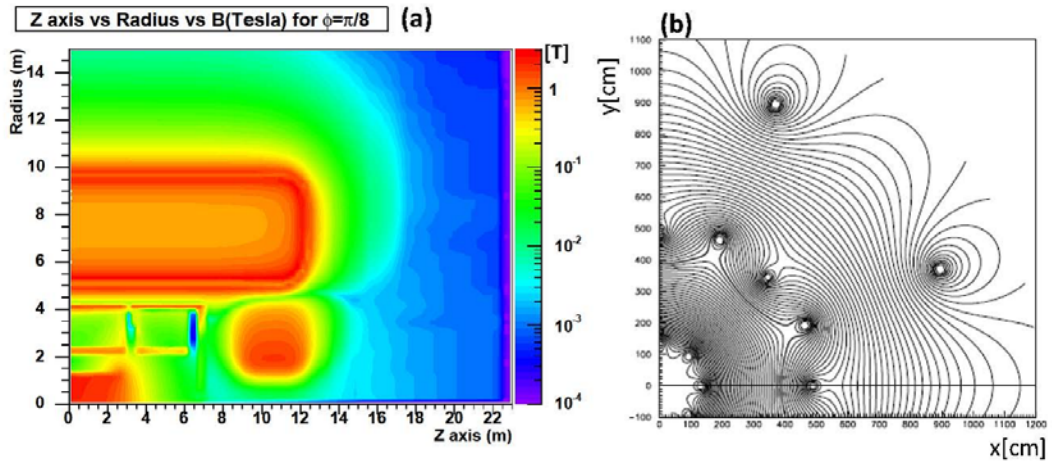

Figure 4.6: Intensity of magnetic field

Because of this reason, it becomes difficult to discriminate a low momentum muon from a high momentum muon.

A histogram in Figure4.7 (b) shows number of muon triggered by muFast on the octant at the threshold of p_T = 6GeV. Even though muon p_T of using sample is 4GeV, there are some muons which are triggered at region where the magnetic field is weak.

If low-p_T muons which do not overreach threshold triggered, trigger rate increases, and this is problem for trigger system.

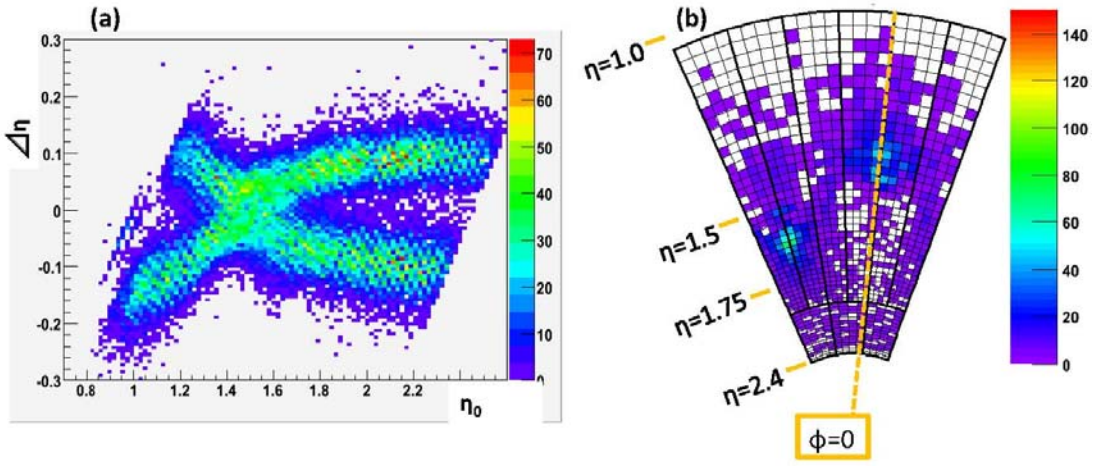

Figure 4.7: (a)Distribution of $\Delta\eta$ (b)Number of triggered muon at p_T threshold is 6 GeV (using p_T=4GeV samples)

4.4 Performance of muFast

For the precise triggering, p_T resolution is an important factor. This is investigated with simulated single muon samples. For each p_T sample

$$\Delta_{p_T} \equiv \frac{1/|p_T^0| - 1/|p_T^{rec}|}{1/|p_T^0|} \tag{4.3}$$

are plotted, where p_T^0 is the generated and p_T^{rec} is reconstructed transverse momentum of muon. Figure 4.8 is for the event whose RoI is barrel, Figure 4.9 is for the event whose RoI is end-cap. For all momentum, the distribution is centered nearly at zero. There are energy loss of muon in the calorimeter of few GeV so that measured momenta at the muon system should be lower. But figures do not show such bias. This means that the effect is implicity corrected by the coefficients. The resolutions is worse for the higher momentum. It is also seen that barrel region has the better resolution than end-cap. In order to make quantitative analysis, the distribution is fitted with Gaussian function. Details of the fitting is described in Appendix A.2.

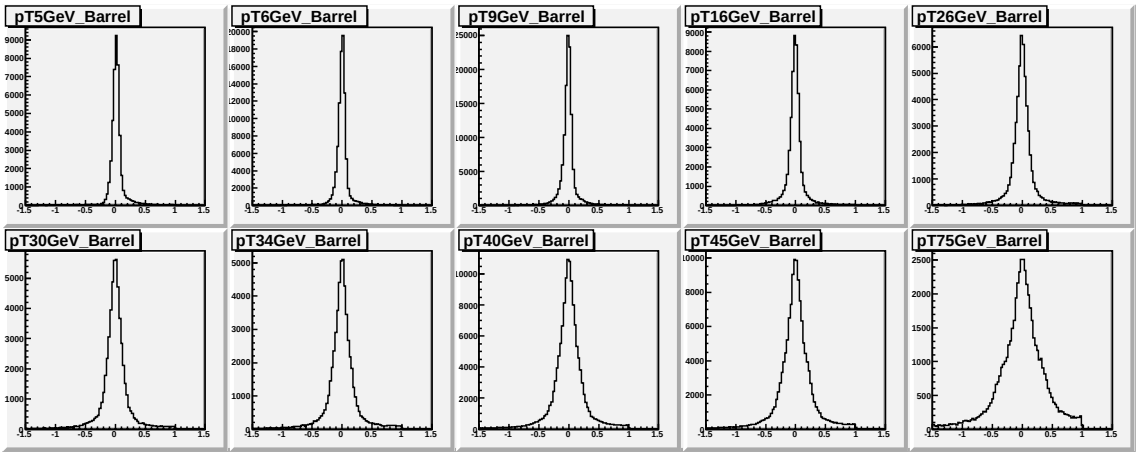

Figure 4.8: Distributions of equation (4.3) at the barrel part

Figure 4.10 left shows the as a function of muon p_T. The black line is for the barrel and red line is for the end-cap. Since α becomes smaller at high p_T the resolution gets worse. At low p_T, the resolution also gets worse because of fluctuation at the energy loss in the calorimeters and the multiple scattering.

Figure 4.10 right shows p_T bias, *i.e.* the center value of the Gaussian fit. Since the LUT are tuned using the Monte Carlo sample whose momenta are 6GeV and 40GeV, p_T

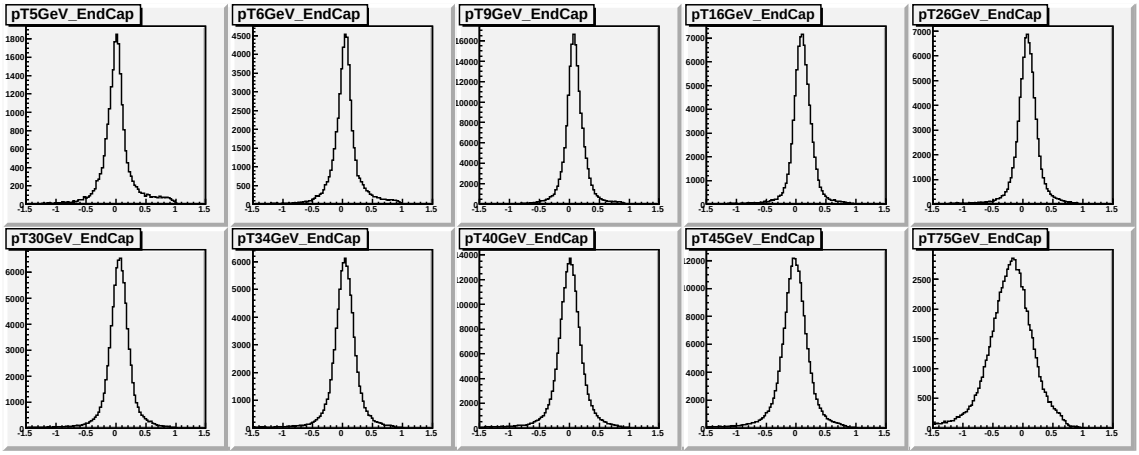

Figure 4.9: Distributions of equation (4.3) at the end-cap part

bias is almost zero at these momenta. But at the other momenta, p_T at the end-cap is deviated by 10 % at p_T = 15 GeV, while p_T at the barrel is deviated less than 1 % at maximum. Since pT can be given in the linear function of radius and the algorithm in the barrel part uses this linear formula, p_T bias at the barrel part is close to zero. On the other hand, linear formula is a simple approximation at the end-cap. This is why p_T bias at the end-cap part is worse than that in the barrel.

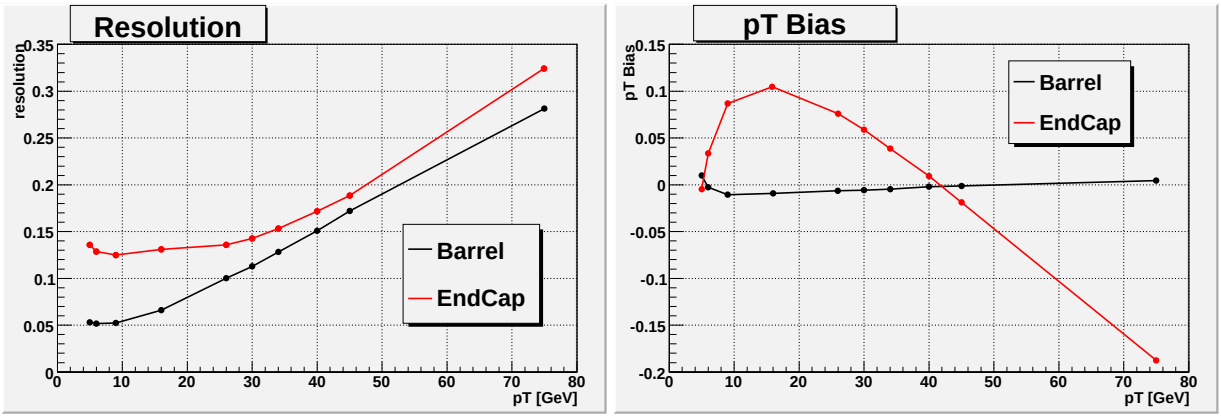

Figure 4.10: Resolutions and p_T biases

Resolution at the end-cap part is worse than barrel region. This is related the inhomogeneity of the field. In order to investigate further, the end-cap is divided into nine regions as shown as in Figure 4.11. The position of each region is shown in Table 4.1.

Region #	(1)	(2)	(3)	(4)	(5)
η	1.05∼1.2	1.2∼1.35	1.35∼1.5	1.5∼1.65	1.65∼1.8
ηBin #	1,2,3	4,5,6,	7,8,9	10,11,12	13,14,15

Region #	(6)	(7)	(8)	(9)
η	1.8∼ 1.95	1.95∼2.1	2.1∼2.25	2.25∼2.4
ηBin #	16,17,18	19,20,21	22,23,24	25,26,27,28

Table 4.1: Definition of regions

Since there are few entries in the first and last η bin (bin 0 and 29), they are not included.

The resolution at each regions are shown in Figure 4.12. It is quite good at region 1, region 7, region 8, region 9. On the other hand, the resolution is worse at region 3 and region 4 where the integrated magnetic field is weak. As seen in section 4.3, the bad regions are more restricted in $\eta \times \phi$ space and they correspond to the regions with low integrated magnetic field.

p_T bias at the end-cap part is also plotted dividing into small region. Figure 4.13 shows p_T bias at each region. p_T bias get worse at region1 and region2.

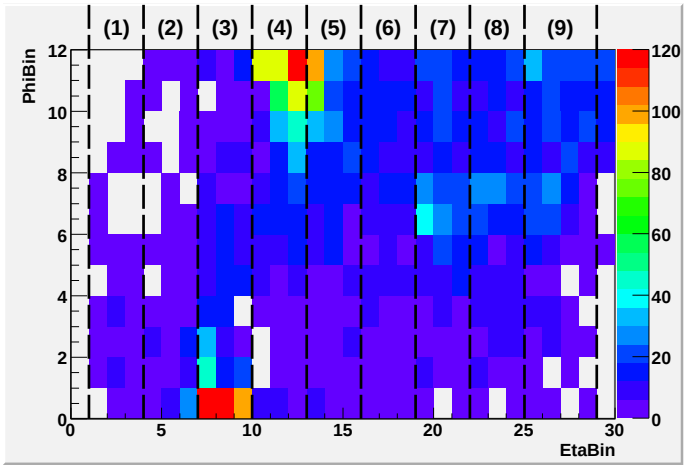

Figure 4.11: Number of L1 triggered events at $p_T = 4$ GeV and procedure of dividing into 9 regions

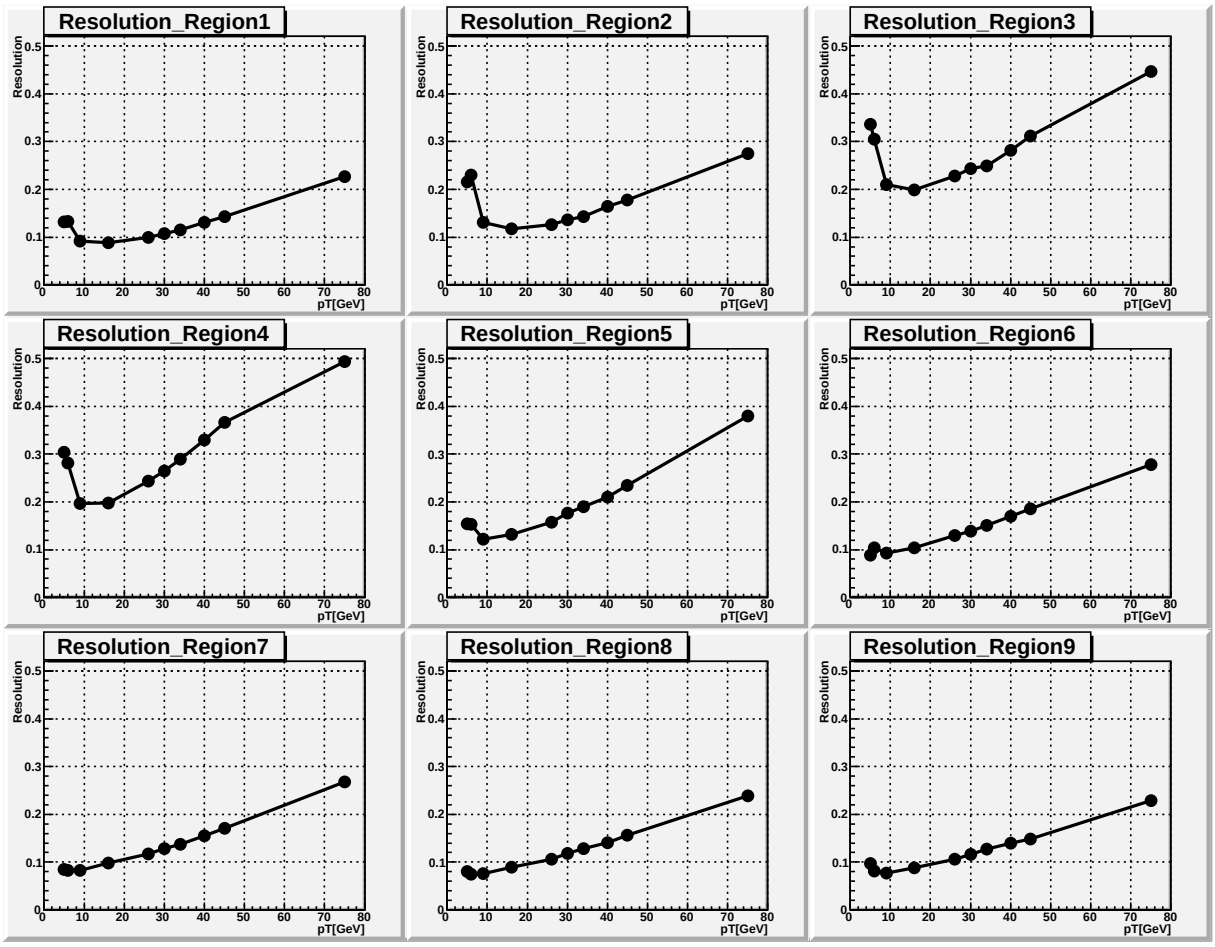

Figure 4.12: Resolutions at each regions

4.5 The correlation between α and vertex spread

In the experiment, the vertex point is not always at origin of the coordinate. It spreads as shown in Figure 4.14 and Figure 4.15. The spread of vertex point in z direction is much wider than that in R direction.

In the muFast, α is determined using nominal vertex point which coordinates (z,R) = (0,0). The effect of the vertex spread are investigated in following procedure.

First, samples are divided into three vertex regions as shown in Figure 4.14. Region (1) is defined with the range of $-3\sigma < z < -\sigma$, region (2) is defined with the range of $-\sigma < z < \sigma$ and region (3) is defined with the range of $\sigma < z < 3\sigma$, where σ is 56 mm. For each sample, the resolution and p_T bias are investigated.

The effect depends on the charge of the muon. Figure 4.16 shows the distribution of

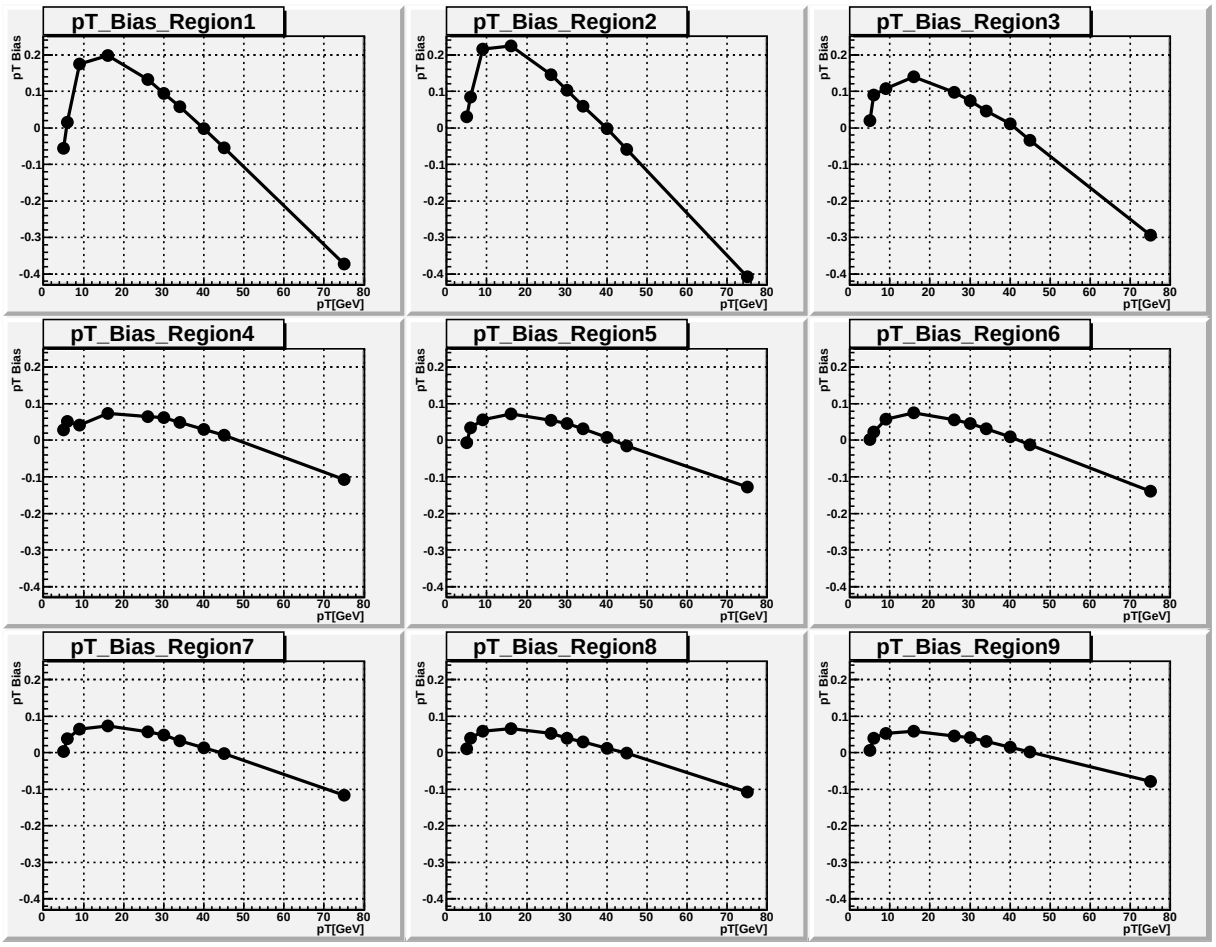

Figure 4.13: p_T bias at each regions

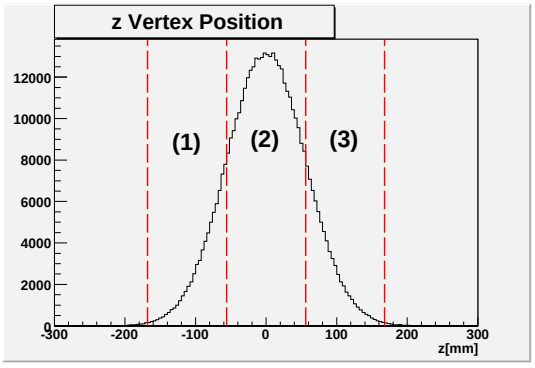

Figure 4.14: Vertex point in z direction

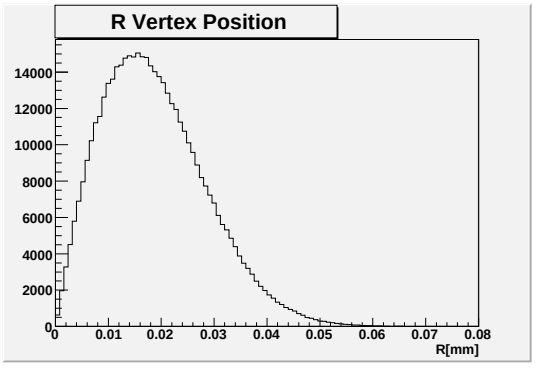

Figure 4.15: Vertex point in R direction

equation (4.3) at each vertex regions with positive charge at $p_T = 75$ GeV. The histogram with black line is made with all entries, red one is made with muons which come from

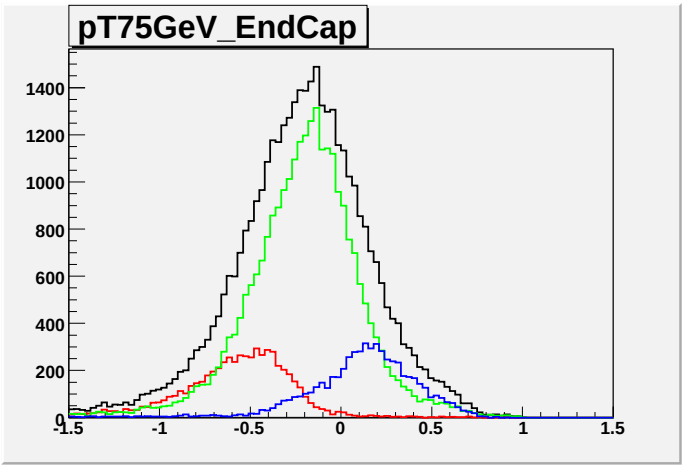

Figure 4.16: Resolutions at each vertex region

vertex region (1), green one is made with muons come from vertex region (2) and blue one is made with muons from vertex (3). Each positions are depend on vertex. The quantitative plots are shown in Figure 4.17 and 4.18.

Figure 4.17 and Figure 4.18 shows resolutions and p_T biases for positive charge. They are plotted at nine η regions which are described in the previous section. Black lines are the result including all sample; *i.e.* the sample line as Figure 4.12 and Figure 4.13. At high p_T, resolutions for each regions are much better than the total and nearly same at three regions. This is also true for the negative muon (not shown). Black line locates at the average of (1), (2) and (3). It is seen clearly that p_T bias correlate with vertex. This is explained as followings. In Figure 4.19, there are two muons. One is generated from the origin of the coordinate (μ_1^+) and the other is generated from point which z coordinate is positive (μ_2^+). Assuming μ_1^+ and μ_1^+ have same p_T and they are both positive charge, α becomes smaller when z position of vertex is bigger than the origin of the point ($\alpha > \alpha'$). If α becomes smaller, reconstructed p_T becomes larger Δ_{p_T} in equation (4.3) becomes larger. If muon has negative charge, α becomes larger and Δ_{p_T} in equation 4.3 becomes smaller. These shift are seen in Figure 4.18. When the z vertex is positive (region(3)), p_T bias shift to larger position.

In summary, the vertex spread is the major contribution in the resolution degrade at the high p_T.

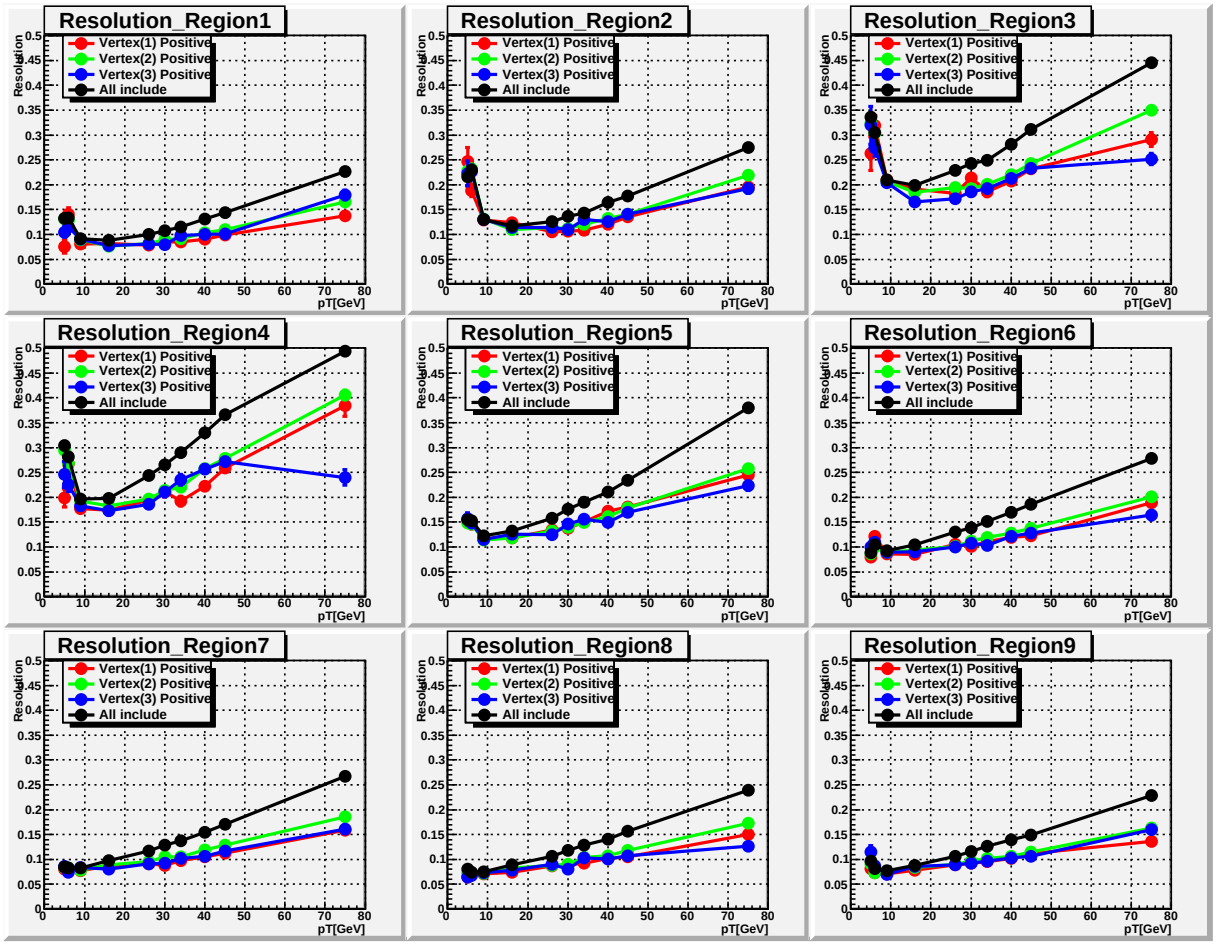

Figure 4.17: Resolutions at positive charge

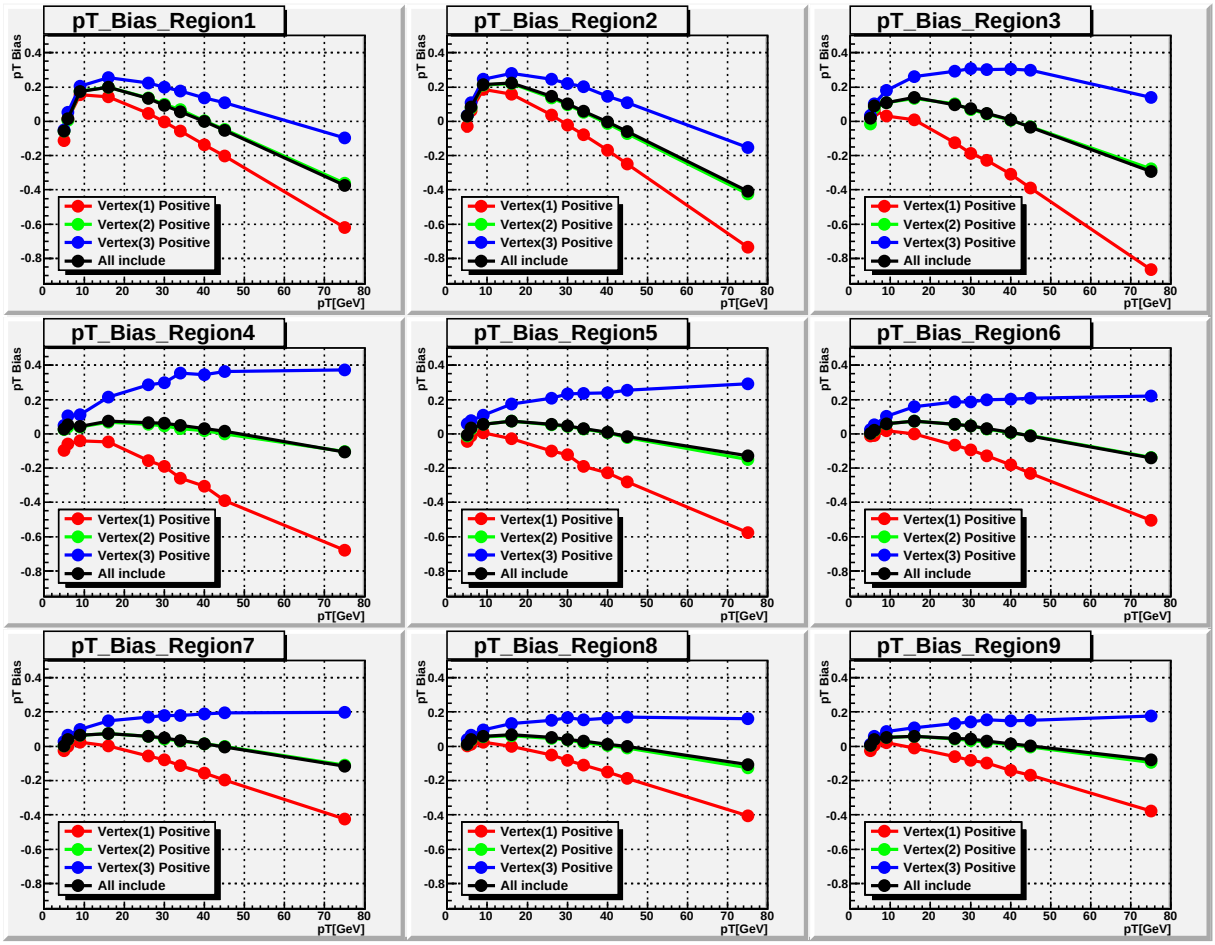

Figure 4.18: p_T bias at positive charge

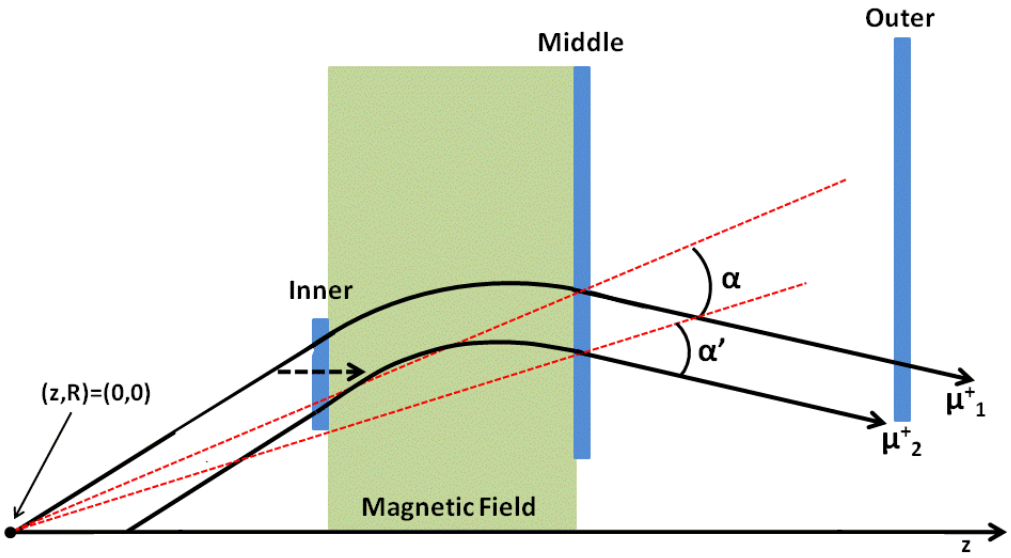

Figure 4.19: Correlation between α and vertex

Chapter 5

New algorithms at end-cap

In Chapter 4, the performance of muFast is investigated, and it is shown that performance of algorithm at the end-cap part is worse than that at the barrel part. For the further improvement two new algorithms for the end-cap part are considered. In this chapter, these new algorithms are introduced and their performance are compared.

5.1 β

One of the idea of new algorithm is using an angle named β which is defined as shown in Figure 5.1. There are two lines in Figure 5.1, one is a line based on the position and direction of a super-point at the inner layer. The other line is drawn with the position and direction of a super-point at the middle layer, or if there is a super-point at the outer layer, the line to connect the two super-points. The angle β is defined as angle between the two lines.

Using β, momentum is described in

$$P = \frac{0.15BL}{\sin(\beta/2)}. \tag{5.1}$$

B is intensity of magnetic field provided by end-cap toroid, L is the effective length of the magnetic field. Using an angle θ_0 defined by the former line, transverse momentum is described in $p_T = P \sin\theta_0$.

Similar to α, p_T is calculated with a linear formula

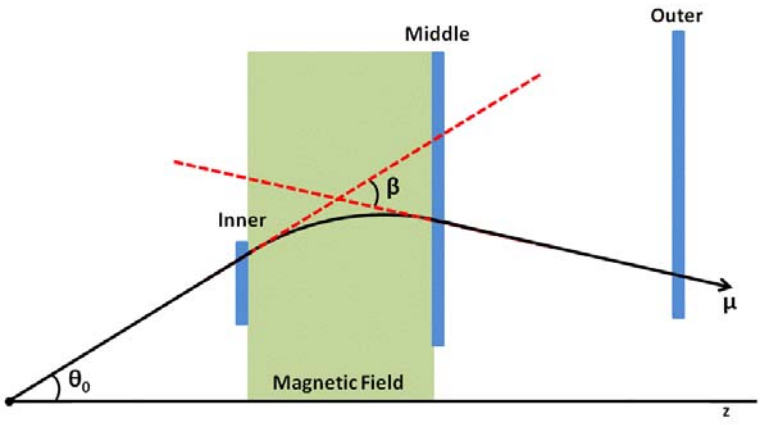

Figure 5.1: Definition of β

$$\frac{1}{p_T} = A_{ij}\beta + B_{ij} \ . \tag{5.2}$$

A_{ij} and B_{ij} are coefficients which are determined in advance. The advantage of β is that β is determined without assuming the vertex point by adding the inner layer hit.

5.2 Sagitta

Another idea is to use *sagitta*. In this analysis, *sagitta* is defined as shown in Figure 5.2. The points of super-point at each layers are named as A, B and C. A point E is defined as the middle point of AB. A line l is drawn from E perpendicular to the line AB. The cross point between the line BC and the line l is set to point D. *sagitta* is defined as length of DE.

Using *sagitta*, momentum is

$$P = \frac{0.15BL}{\sin\{\tan^{-1}(2S/L)\}}.$$

Definition of B and L is same as equation 5.1. To save the computation time at L2 trigger, p_T is calculated again with linear formula

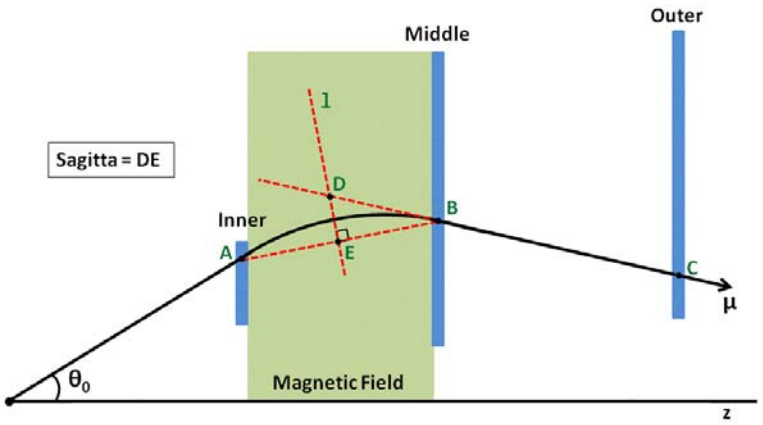

Figure 5.2: Definition of sagitta

$$\frac{1}{p_T} = A_{ij}S + B_{ij}. \tag{5.3}$$

As the case of β, *sagitta* can be determined without assuming the vertex point. In principally, *sagitta* is also determined using the position of a super-point at inner layer and position and direction of a super-point at middle layer. In this study, however performance of *sagitta* determined from position information only are investigated. Therefore it is required a hit in each three layers. By avoiding for the use of the direction information, errors from wrong track pattern recognition may be eliminated.

5.3 Comparing new algorithms

5.3.1 Calibration

To compare performances for each algorithms, it is required to determine coefficients A and B for α, β and *sagitta* in advance. For this purpose, a large number of single muon Monte Carlo events are generated with p_T = 9 GeV and 45GeV. The values of α, β or *sagitta* is calculated for each $\eta \times \phi$ bin. Whole range of the octant in η direction is divided into 30 bins and half range of the octant in ϕ direction is divided into 12 bins as same

procedure as which described in section 4.2.

Using the distribution of variables (α, β and *sagitta*), the center values for each momentum are determined. Example of the distribution is shown in Figure 5.3. From center values of the two p_T values, A_{ij} and B_{ij} are obtained. If there are no entries in a bin with one p_T sample, A_{ij} is determined solely with the center position of another p_T sample, by setting $B_{ij} = 0$. If there are no entries from the both samples, both coefficients will be zero.

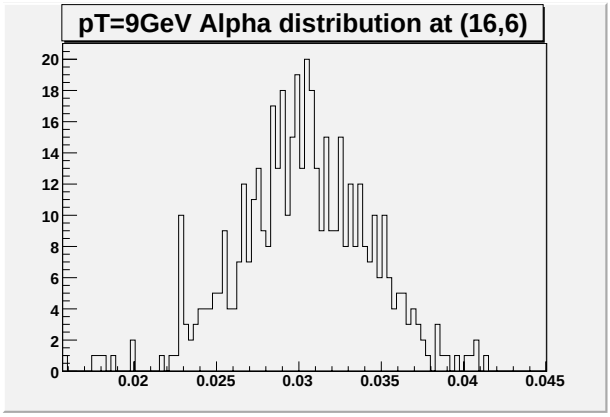

Figure 5.3: Distribution of α at (ηbin,ϕbin) = (16,6) when p_T = 9GeV

Used samples

Figure 5.4 shows number of muon entries at each bins. The left histogram shows number of muon entries using 6 GeV single muon sample, and the right histogram shows number of muon entry using 9 GeV single muon sample. Since muons which p_T is 6 GeV are bended more than those which p_T is 9GeV, the $\eta\phi$ distribution of 6 GeV p_T sample distribute less uniform than those of 9 GeV sample. Lower p_T muons tend to be focused at the region which magnetic field is weak. There are few entries at region where $\eta bin < 5$. For this reason, coefficients are calculated using single muon sample of 9 GeV and 45 GeV. (LUT in muFast is calculated using sample of 6 GeV and 40 GeV.)

Each single muon samples contain approximately 500,000 events for each p_T.

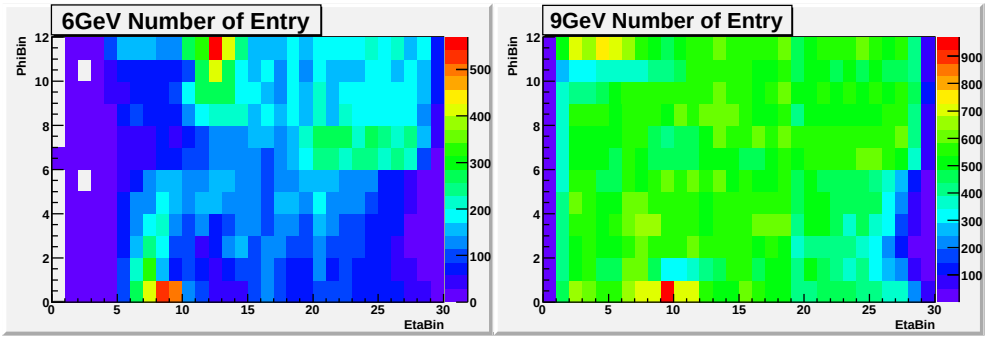

Figure 5.4: Number of entries

Determination of the center value

For determination of the center values of the variables (x = α, β or *sagitta*) for each η bin, three procedures are evaluated, mean, Gaussian fit and Gaussian fit with charge separation.

The first one is using a simple mean value of all entries. The mean value is defined as

$$\frac{1}{n}\sum_{i=1}^{n} x_i,$$

where n is number of entries in the $\eta \times \phi$ bin. One option is to use this mean value as the center values of each $\eta \times \phi$ bin.

Other two procedures use Gaussian fittings. One is considering sign of variables, and the other does not consider sign. At the region where the magnetic field is weak, α, β and *sagitta* values become small. Since these variables are currently defined as positive values, *i.e.* they do not have negative values, the distribution has a shape cut at 0 as seen in Figure 5.5 (a). Since it is not appropriate to fit such histogram with Gaussian function, the sign is introduced to these three variables. The definition of these sign is following; the sign is positive when muon is bended to the direction where $|\eta|$ increases, and the sign is negative when muon is bended to the direction where $|\eta|$ decreases. The histogram (b) in Figure 5.5 shows distribution of α with sign at same region as (a) using positive charged single muon sample.

There are totally 360 bins at the end-cap. It is difficult to make histogram and fit them manually. Therefore, histograms are made and fitted automatically. But fitting is significantly affected by the fitting range and the bin width. Hence, automation need

to be done carefully. The procedure of making histograms and fitting are described in Appendix A.

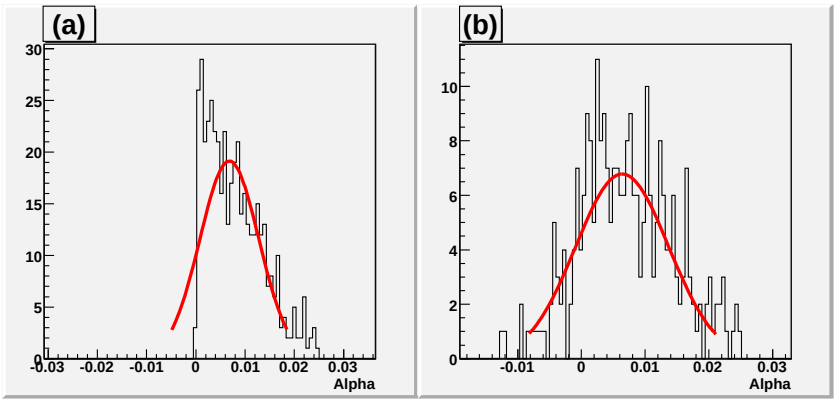

Figure 5.5: Distribution of α using $p_T = 9$ GeV samples at the region where the intensity of magnetic field is weak

Figure 5.6 shows resolutions and p_T bias of each calculation procedure with algorithm of α. The graph drawn with black line is one which is calculated using p_T reconstructed muFast, *i.e.* LUT is already determined as the ATLAS standard. (The LUT is tuned with the Monte Carlo samples of 6 GeV and 40 GeV.) Both resolution and p_T bias of method using mean value are bad. Considering sign do not affect a lots to the resolution and p_T bias. In the further, coefficients are calculated in the method which do not consider sign.

Comparing resolution using coefficients from Gaussian fitting and those already in the muFast, resolution of the original muFast is better. The more sophistical procedures might be needed for automatic determination of the coefficients.

Since tuning is done at $p_T = 9$ and 45 GeV, p_T biases using Gaussian fitting is close to zero at these p_T.

5.3.2 Comparison of the performance

Using the coefficients determined with the procedure described in the last section, p_T is reconstructed with α, β and *sagitta*. The resolution and p_T bias are investigated.

In *sagitta* calculation, a super-point must exist at every layer. To make a fair comparison the same sample is used for the performance study of α, β and *sagitta*. Figure 5.7 shows the efficiency to have at least one hit in each layer. The Efficiency is over 90 %

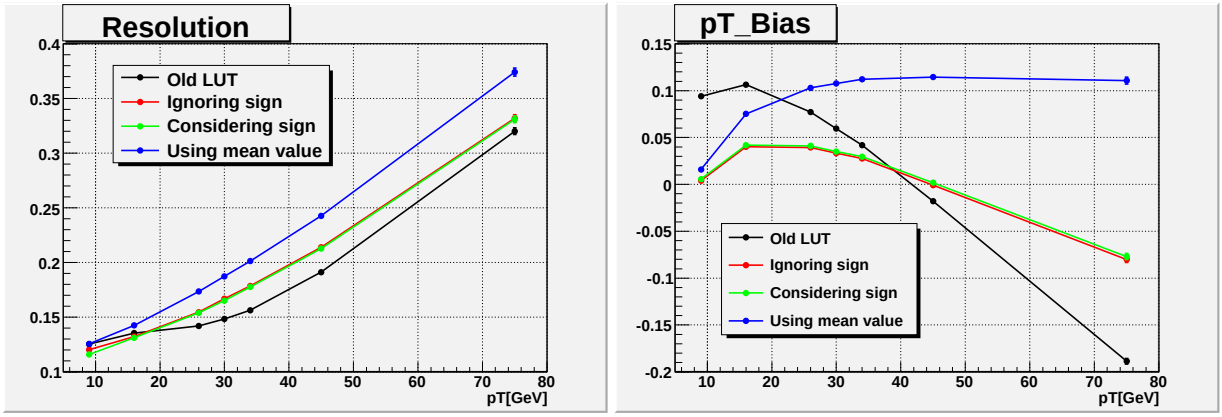

Figure 5.6: Resolutions and p_T biases calculated in each method

for bin 7 $\sim$ bin 18 of η. For this reason, comparing is done in this region ($7 \leqq \eta bin \leqq 18$). These are assigned as region 3, 4, 5 and 6 in Figure 4.11.

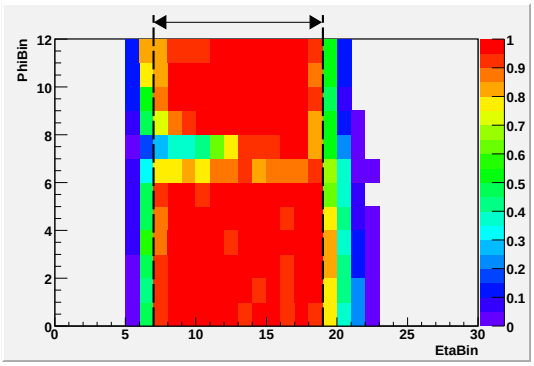

Figure 5.7: Ratio of the entries which have three hits at each layer

Resolution and p_T bias

Resolution and p_T bias are calculated for α, β and *sagitta*, using with the same procedure described in section 4.3. Figure 5.8 shows the resolutions and Figure 5.9 shows the p_T bias. Four graphs corresponds to the each regions. Resolutions and p_T bias of the original muFast (described as "Old LUT") are also plotted as a reference.

Generally β and *sagitta* gives the better resolution than α. For region 4, β gets worse as α. p_T bias given by each variables are close to zero at $p_T = 9$ GeV and $p_T = 75$ GeV which are tuning point, and they are all similar.

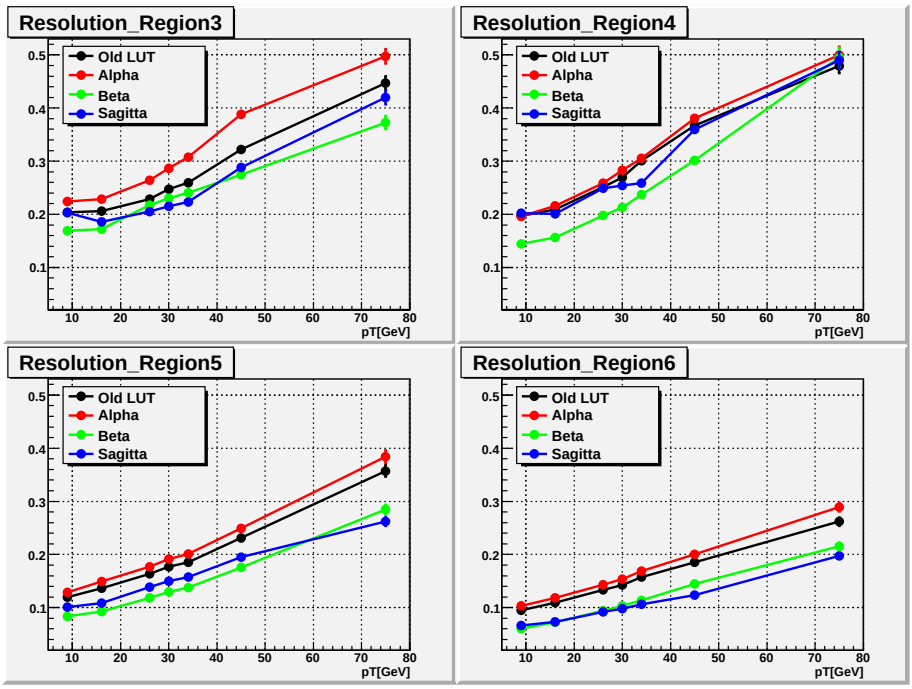

Figure 5.8: Resolutions at each region

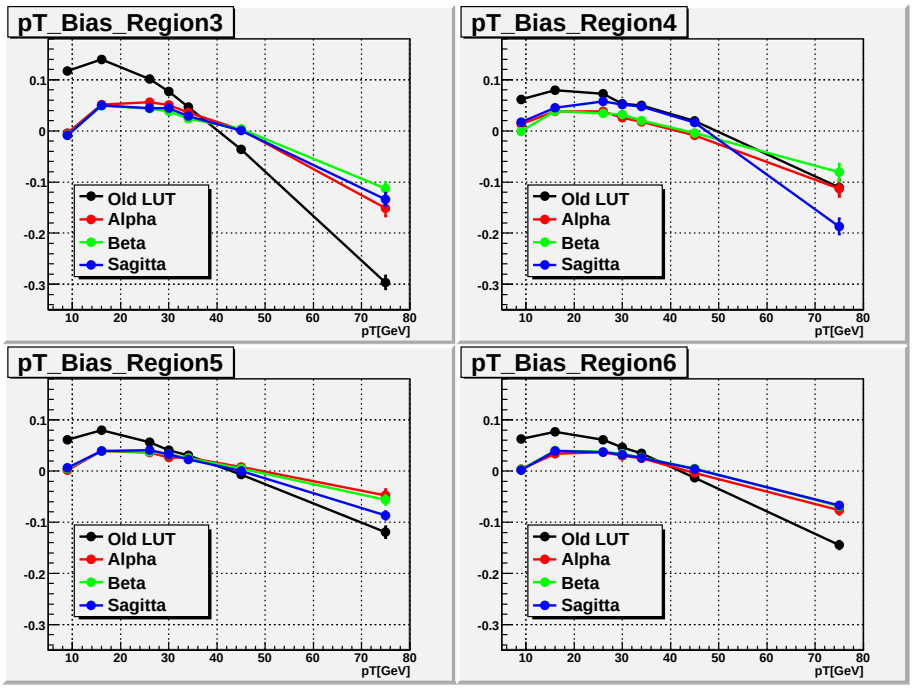

Figure 5.9: p_T bias at each region

Distribution

In the previous subsection, the resolution are measured in term of σ in the Gaussian fit. However, as seen in Figure 5.10, there are wider tails in the distributions of Δ_{p_T}.

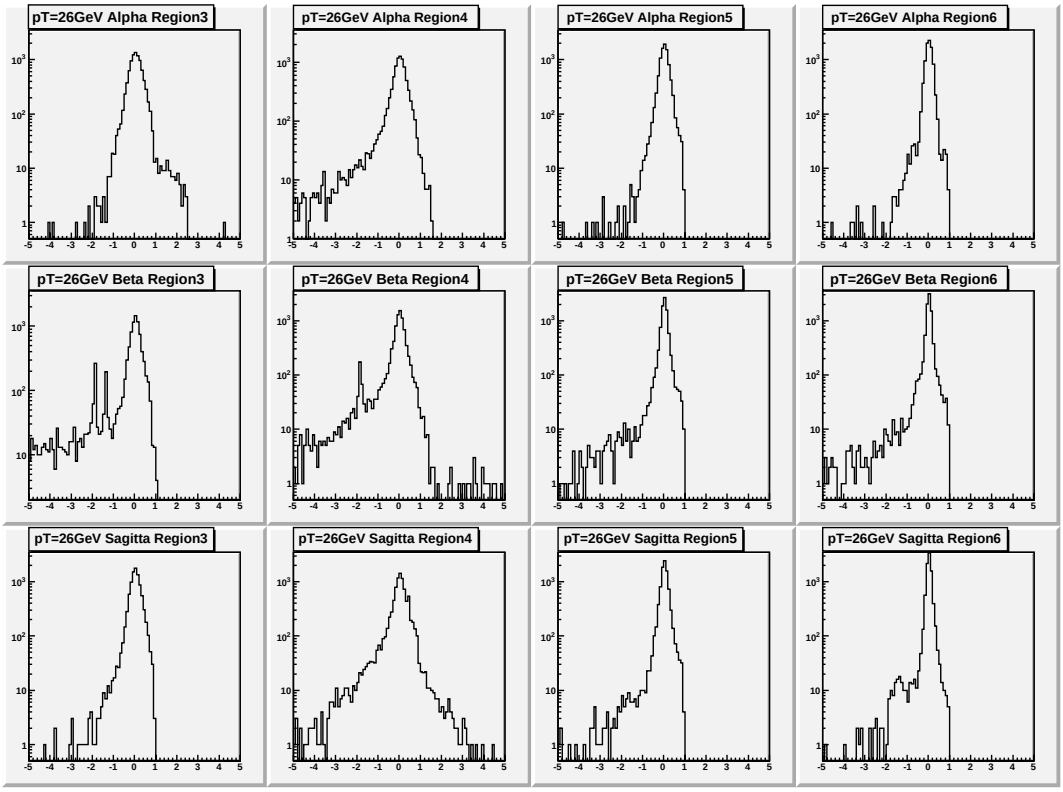

Figure 5.10: Distribution of equation (4.3) at $p_T = 26$ GeV

There looks more tails in the distribution by β than that by α and *sagitta*. There is a strange peaks in the case β. It turns out that these events come from bins where coefficient A_{ij} is unreasonably small and B_{ij} is large so that calculated p_T is almost same independent to the value of β. Determination of coefficients are missed there. This means the automation fitting procedure need more improvement.

To estimate the quantitatively, a fraction of events in the tail are plotted in Figure 5.11. From the upper to lower figures shows fractions of events out of 2σ, 3σ and 4σ from the center.

In the region3 and 4, the fraction of events with α and *sagitta* decrease as the range is set wider, but the fraction of events with β decreases very slowly. This is because of the peaks as already described. Even for the other regions, the fraction of tail events with

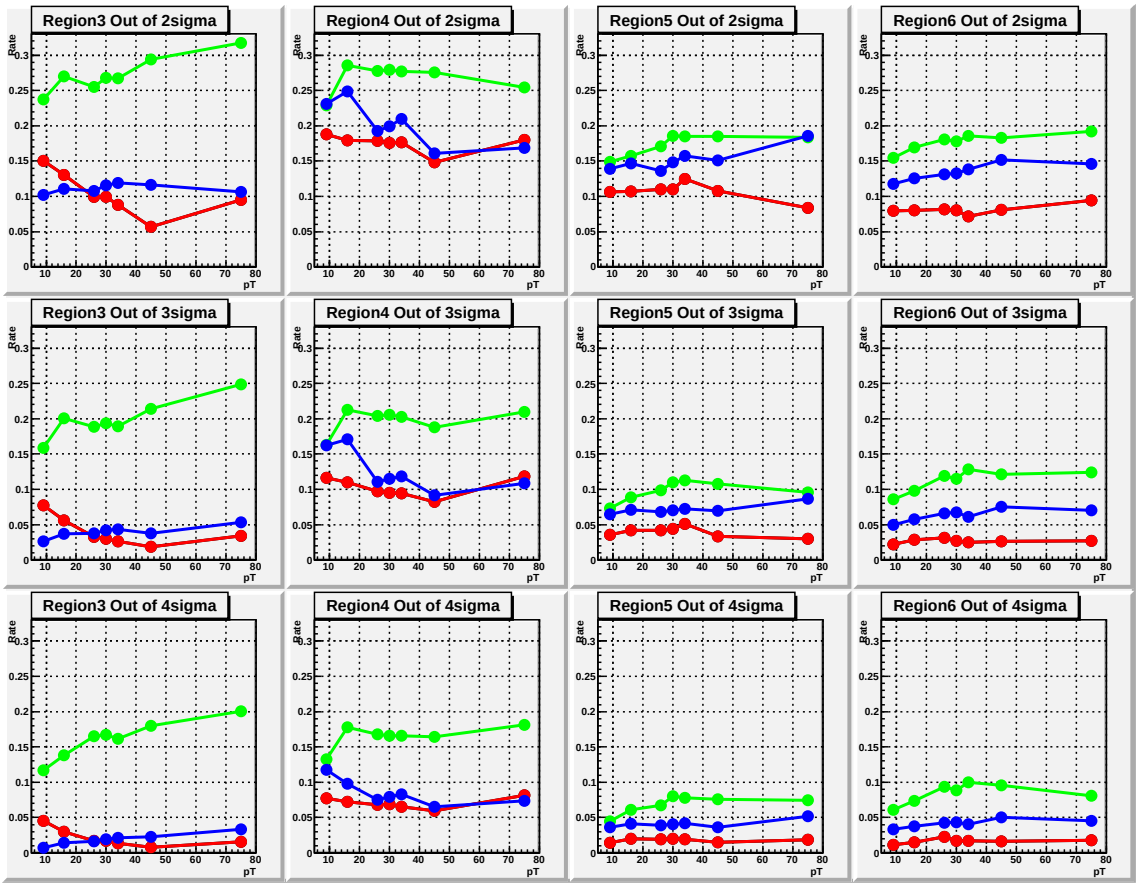

Figure 5.11: Ratio of tails: Red is ratio using α, green is ratio using β and blue is ration using *sagitta*

β is still higher than the others. From Figure 5.11 it is seen that this fraction mainly comes from the tails in the negative side. Therefore p_T is underestimated and the trigger efficiency is deteriorated.

An example, trigger efficiencies for 45 GeV muon when p_T threshold is 20 GeV are calculated as shown in Table 5.1. It is shown that efficiency with β is worse than the others. This is the effects of the tails.

Efficiencies as a function of muon p_T for region 5 and 6 are shown in Figure 5.12. The p_T threshold is set to 20 GeV. The efficiency is defined with respect to muons with hits at all three layers. Because of the tails described in the previous subsection, the efficiencies using β and *sagitta* are lower than those using α for muons with $p_T \geq 20$ GeV. Those using β is lowest. On the other hand, muons with p_T lower than the threshold are better killed with the algorithms using β and *sagitta* than the one using α.

	Region3	Region4	Region 5	Region6
α	98.922±0.11840	93.107±0.29280	99.004±0.11519	99.009±0.11462
β	(82.950±0.43119)	(84.358±0.41985)	95.855±0.23123	96.157±0.22247
sagitta	98.002±0.16045	93.214±0.29069	98.035±0.16100	97.978±0.16287

Table 5.1: Efficiency at each region (%)

Figure 5.13 is the similar efficiency plot, but in this time, the efficiencies are calculated with respect to all muons which hit the RoI in the region 5 and 6. In this case, the inefficiency due to the missing hits are also seen. Since α can be calculated only with middle layer hit, the efficiencies remains high. On the other hand, since *sagitta* requires a hit at every three layers, efficiencies become lower but still comparable with β.

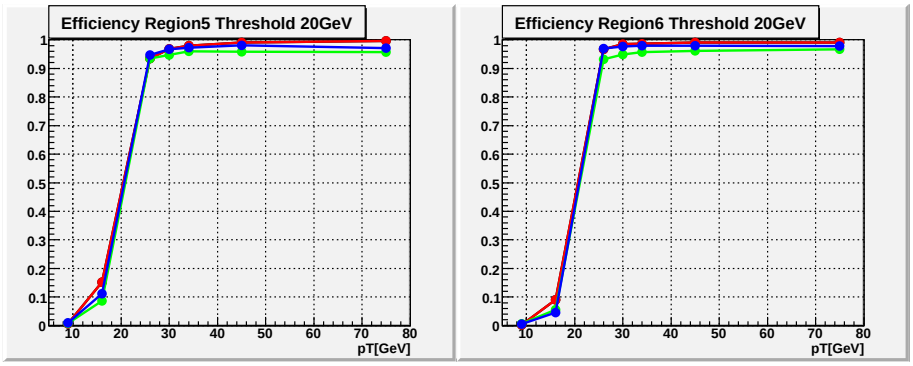

Figure 5.12: Efficiencies at region 5 and 6 using muons with a hit at every three layers: Red is those using α, green is those using β, blue is those using *sagitta*

5.3.3 The correlation between β, *sagitta* and vertex spread

The correlation between β and vertex position or *sagitta* and vertex position is investigated. Resolution and p_T bias are plotted at each region as same procedure as described in section 4.4.

Figure 5.14 and Figure 5.15 shows resolutions given by β. Both positive charge and negative charge are plotted together. Resolutions are nearly same at each vertex region and charge. This indicates p_T biases does not depend on the vertex position. But they depend on the charge at region 5 and 6. The reason why β is depend on charge will be

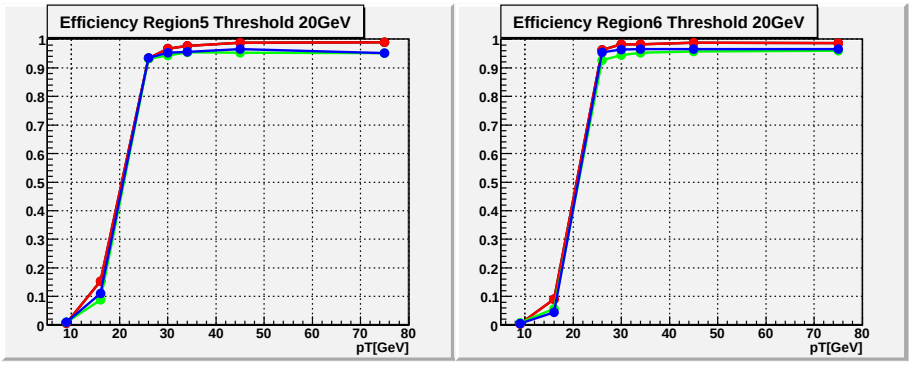

Figure 5.13: Efficiencies at region 5 and 6: Red is those using α, green is those using β, blue is those using *sagitta*

investigated.

Figure 5.16 and Figure 5.17 shows resolutions given by *sagitta*. Resolutions are nearly same, and p_T biases do not depend on vertex or charge.

All this show that p_T determination with β and *sagitta* is less affected by the vertex position and that β and *sagitta* gives a better resolution than α at the high p_T.

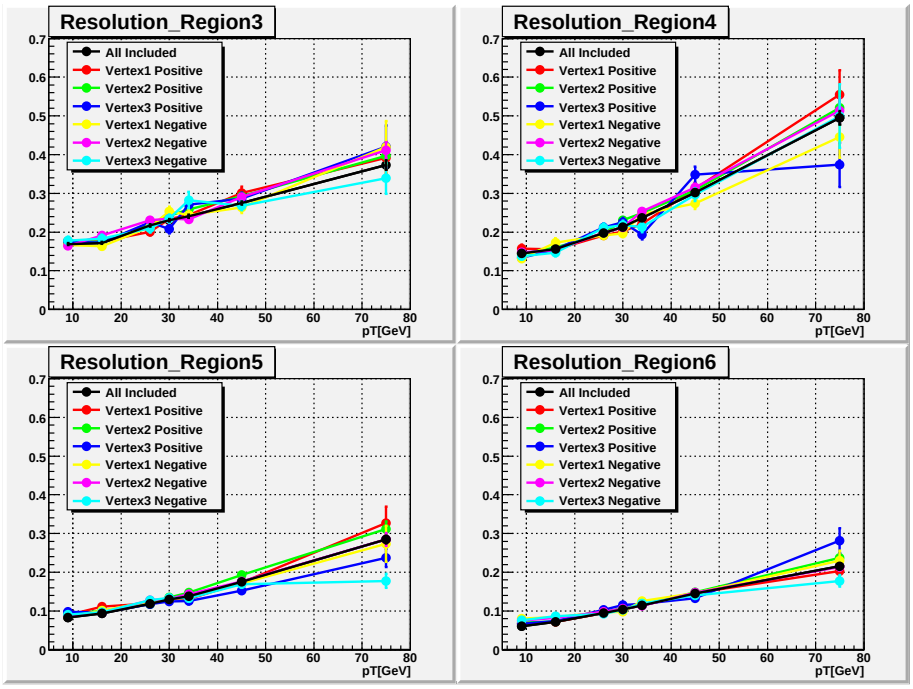

Figure 5.14: Resolution given by β divided by vertex

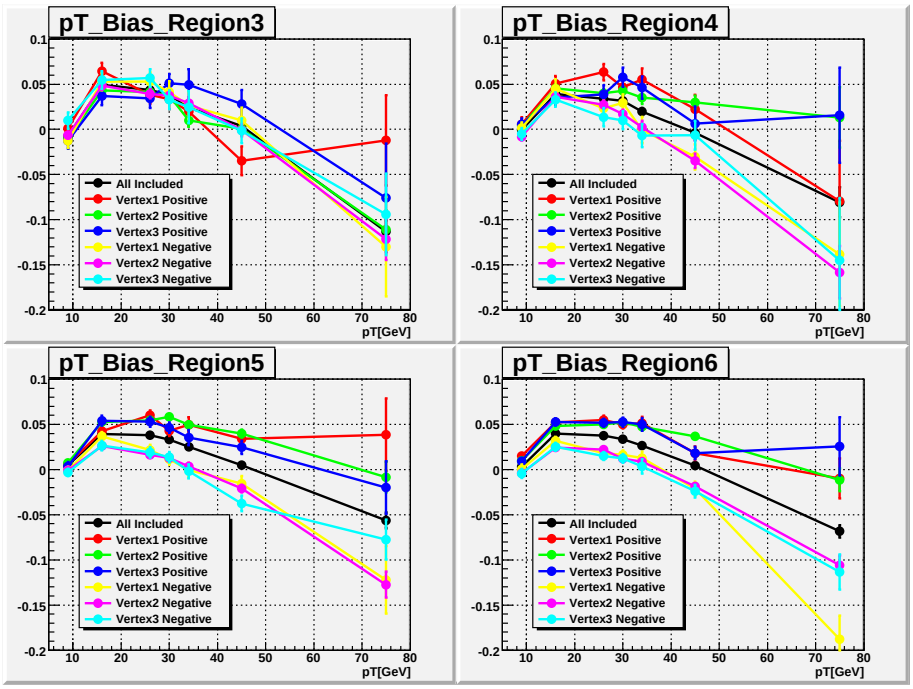

Figure 5.15: p_T bias given by β divided by vertex

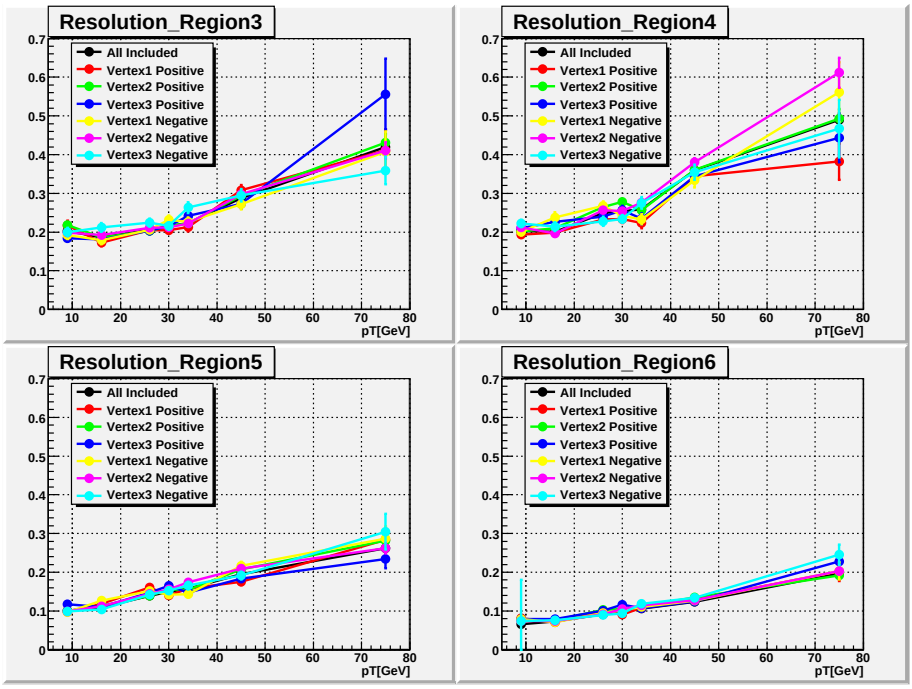

Figure 5.16: Resolution given by *sagitta* divided by vertex

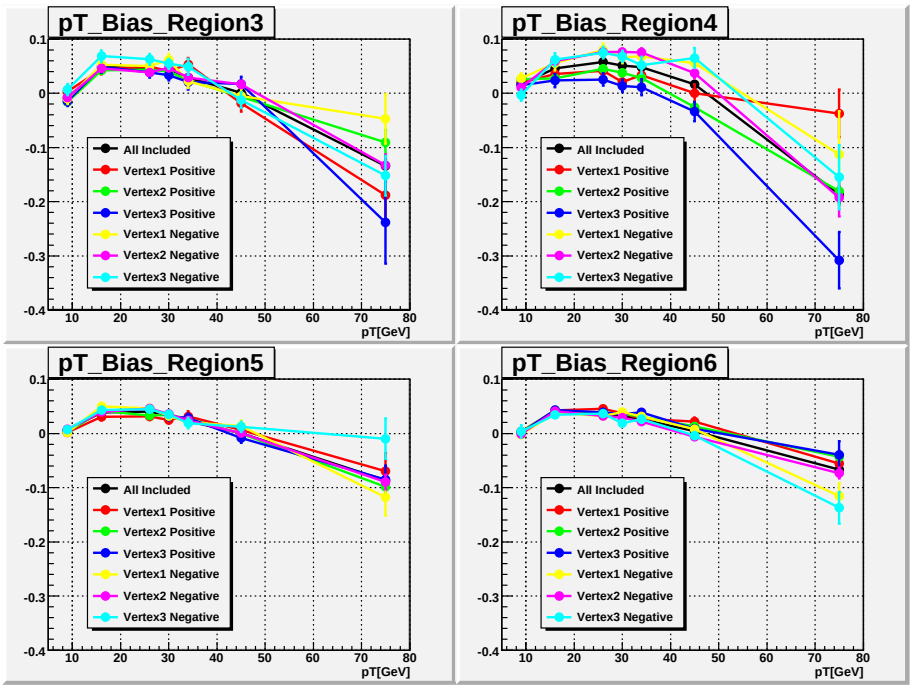

Figure 5.17: p_T given by *sagitta* divided by vertex

Chapter 6

Summary

The performance of Level2 ATLAS muon trigger was investigated. The examined are the algorithm called muFast which uses information of muon system only.

Since the algorithm at barrel uses radius (R) to reconstruct p_T, the p_T bias at the barrel are better than that in the end-cap. At the end-cap, since the algorithm at the end-cap is using an angle α, the p_T bias is worse than that at the barrel. Resolutions at the region where include nonuniform magnetic field is worse than the others. Since α is determined using nominal vertex, resolution and p_T bias are affected by the vertex position.

For the further improvement, two new algorithms for the end-cap are introduced. One is using an angle β and the other is using a length *sagitta*, requiring more hit point in the muon chambers.

To compare these algorithms, calibrations are done. Using Gaussian fitting or mean deviation of the histograms, the coefficients for the reconstruction of p_T are determined. The end-cap is segmented into bins, and these coefficients are determined for each bin.

For the reconstructed p_T, resolution and p_T bias are compared. The data where super-points are measured in all inner, middle and outer layer are used for the comparison. These regions are divided into four regions. At each region, four resolutions using algorithms with β and *sagitta* are better than that using algorithms with α. p_T biases using each algorithms are all similar.

α gives generally good performance. Measured p_T with the angle α has a strong dependency on the vertex position. β gives good resolutions, but its distribution has longer tails than others. *sagitta* also gives good performance, but a super-point must

exist every layer to determine *sagitta* and these regions are small.

By developing algorithms which use these variables combined, it is expected that the performance of muFast improves. On the other hand, the automation of determining center value needs more improvement.

Appendix A

Making histograms and fittings

The bin width of histogram is determined and fitted in following procedure.

A.1 Making histograms

Histograms are made and fitted once. After the fitting, histogram is remade and fitted again. The range of the first histogram is made using mean value $\bar{x}$ and standard deviation (SD) σ_{SD} determined using all entries at the bin. $\bar{x}$ and σ_{SD} are defined as following;

$$\bar{x} = \frac{1}{n}\sum_{i=1}^{n} x_i,$$

$$\sigma_{SD} = \sqrt{\frac{1}{n}\sum_{i=1}^{n}(x_i - \bar{x})^2}$$

where n is number of entries at each bins. The minimum (x_{min1}) and maximum (x_{max1}) of the histogram is set to

$$x_{min1} = \bar{x} - 5 \times \sigma_{SD},$$

$$x_{max1} = \bar{x} + 5 \times \sigma_{SD}.$$

Then histograms are filled. If number of entries at a bin are over 50 (Case A), histogram is fitted with Gaussian function in the method as described in next section. If number of entries at a bin are less 50, histogram is not fitted (Case B). Histograms are remade using

mean (x_{mean}) and σ_{gauss} of Gaussian fit or mean value of histogram $\bar{x}_{hist}$ and standard deviation of histogram σ_{SD}^{hist}. In Case A, x_{min2} and x_{max2} are set to

$$x_{min2} = x_{mean} - 4 \times \sigma_{gauss},$$

$$x_{max2} = x_{mean} + 4 \times \sigma_{gauss}.$$

In Case B, they are set to

$$x_{min2} = \bar{x}_{hist} - 5 \times \sigma_{SD}^{hist},$$

$$x_{max2} = \bar{x}_{hist} + 5 \times \sigma_{SD}^{hist}.$$

In Case A, histograms are fitted again and mean of Gaussian is used for the center value. In Case B, mean value of the histogram remade is used for the center value.

A.2 Fittings

Fitting is done twice at one step. First fitting is done with Gaussian function within the range between x_{min1} and x_{max1} which are defined as

$$x_{min1} = \bar{x} - 2 \times \sigma_{SD},$$

$$x_{max1} = \bar{x} + 2 \times \sigma_{SD}.$$

Gaussian function is described in

$$f(x) = \frac{1}{\sqrt{2\pi}\sigma_{gauss}} exp\{-\frac{(x-\mu)^2}{2\sigma_{gauss}^2}\},$$

where μ is the center value of Gaussian function.

Then second fitting is done with Gaussian function within the range between x_{min2} and x_{max2} which are defined as

$$x_{min2} = \mu - 2 \times \sigma_{gauss}$$

$$x_{min2} = \mu + 2 \times \sigma_{gauss}.$$

Then μ and σ_{gauss} are used as the result of fitting.

Bibliography

[1] LHC Design Report,
http://ab-div.web.cern.ch/ab-div/Publications/LHC-DesignReport.html

[2] The ATLAS Experiment at the CERN Large Hareon Collider,
ATLAS Collaboration

[3] CMS Technical Proposal, CERN-LHCC-94-38,CMS Physics TDR,
CERN-LHCC-2006-001

[4] ALICE Technical Proposal, CERN-LHCC-95-71,
ALICE : Physics Performance Report, 2004 J. Phys. G: Nucl. Part. Phys. 30(2004) 1517-1763

[5] LHCb Technical Proposal CERN-LHCC-98-4

[6] S.Weinberg: Phys. Rev. Lett. 19(1967) 1264

[7] Physics of and with Leptons WS 05/06 -Feynman Graphs http://pi.physik.uni-bonne.de/ book/feynman/vtp_ws0506

[8] ATLAS Japan,Collection of SM pictures
http://atlas.kek.jp/sub/photos/Physics/PhotoPhysicsSM.html

[9] ATLAS Technical Design Report
ATLAS Level-1 Trigger Group

[10] Event Filter TrigMoore documentation
http://twiki.cern.ch/twiki/bin/view/Atlas/MuonTriggerDocEFTrigMoore

Acknowledgment

First of all, I am really grateful to my supervisor Prof. K.Tokushuku for his all support to my studying and to my life at graduate university and CERN. Without his great support I am not be able to do anything. Thanks to his solicitude, I could concentrate my studying without any problems.

I also would like to appreciate Dr. K.Nagano for his various support and advice. His great advice from close point of view helped me in a lot of situations.

I would like to thank Dr. K.Ozone for his lots of help. Thanks to his help not only in studying but also in the life at CERN, I could spend wonderful life in CERN.

I am grateful to Mr. C.Omachi and H.Kiyamura for their advice as same student. They treat me as colleague and it was great helpful for me.

I also appreciate members of ATLAS HLT Japan group group for great advise. And I also appreciate members of ATLAS Japan group for their support.

I would like to thank Mr. Y.Ri, Mr. R.Hori, Ms. S.Shimizu and Ms. N.Okazaki for their variety of advice and opinion. Even though they work different experiment, their support and advice are very helpful for me.

I am pleasure to study with Mr. R.Yonamine, Mr. Y.Suzuki and Mr. Y.Takahashi. At last, I sincerely thank to my family and Chiaki for being so understanding and warm support.